Scientific Reports

https://doi.org/10.1038/s41598-026-64505-9

Article in Press

Updated comprehensive probabilistic seismic hazard analysis of the Andaman-Nicobar and Sumatra regions

Received: 18 March 2026

Accepted: 27 July 2026

Published online: 07 August 2026

Cite this article as: Saini S., Shahabuddin M. & Roy P.N.S. Updated comprehensive probabilistic seismic hazard analysis of the Andaman-Nicobar and Sumatra regions. *Sci Rep* (2026). https://doi.org/10.1038/s41598-026-64505-9

Saurabh Saini, Mohd Shahabuddin & Paresh Nath Singha Roy

Updated Comprehensive Probabilistic Seismic Hazard Analysis of the Andaman-Nicobar and Sumatra Regions

Saurabh Saini[1]*, Mohd Shahabuddin[1]*, Paresh Nath Singha Roy[1]

[1] Department of Geology and Geophysics, Indian Institute of Technology Kharagpur, Kharagpur, West Bengal, 721302, India

* Correspondence to: saurabhsaini01998@gmail.com; mohdshahabuddin3@gmail.com

Abstract

The Andaman-Sumatra subduction zone is among the most seismically active regions on Earth and has generated several great earthquakes ($M_w \geq 8.0$) in recent decades. This study presents an updated probabilistic seismic hazard assessment (PSHA) for the Andaman-Nicobar and Sumatra regions using a homogenized earthquake catalog spanning 1881-2025 comprising 37,660 events compiled from multiple global and regional agencies. The catalog was homogenized to moment magnitude (M_w) using region-specific conversion relations, declustered using established techniques, and evaluated through temporal and magnitude completeness analyses. Seismic sources were represented using three complementary approaches: tectonically defined areal source zones, fault-based linear source zones, and a gridded point source model constructed on a 0.1° × 0.1° spatial grid. Seismicity parameters were estimated using source specific magnitude of completeness (M_c) values derived from frequency-magnitude distribution analysis. Four ground motion prediction equations (GMPEs) were selected from an initial set of eleven through statistical evaluation of strong motion records and weighted using a log-likelihood approach. Epistemic uncertainties were incorporated through a 72-branch logic tree framework. The resulting hazard maps indicate peak ground acceleration (PGA) values of 0.25-0.40 g for 10% probability of exceedance (PoE) in 50 years, increasing to 0.40-0.70 g for 2% PoE along the Sunda megathrust and Nicobar segment. The results highlight the significant seismic hazard associated with both megathrust and intraplate sources and provide an improved regional hazard framework for engineering design and seismic risk mitigation.

Keywords: Probabilistic seismic hazard assessment; Andaman-Sumatra subduction zone; Sunda megathrust; seismic sources; seismicity; ground motion prediction equations; peak ground acceleration; spectral acceleration.

Introduction

Subduction zones are among the most seismically active regions on Earth and generate nearly 80% of the world's largest earthquakes, particularly megathrust events with $M_w \geq 8.0$[1,2]. Major megathrust earthquakes, including the 1960 Chile, 2004 Sumatra-Andaman, and 2011 Tohoku events, have demonstrated the catastrophic potential of subduction zone seismicity and its implications for regional seismic hazard assessment.

The Andaman-Sumatra subduction zone represents a highly complex tectonic environment, resulting from the oblique convergence of the Indo-Australian Plate beneath the Burma-Sunda Plate. Geodetic observations indicate significant along-strike variation in convergence rates, ranging from about 5.7 cm/yr near Java to about 3.9 cm/yr in the Andaman sector[3,4]. The convergence azimuth also varies significantly, ranging from almost orthogonal in the southern part to almost trench-parallel near the Andaman Islands[5]. These variations strongly influence rupture segmentation and regional seismic hazard.

Since the beginning of the 21st century, the Andaman-Sumatra region has experienced multiple great earthquakes ($M_w \geq 8.0$), establishing it as one of the most seismically hazardous regions on Earth. The December 26, 2004 Sumatra-Andaman earthquake (M_w 9.0-9.3) ruptured more than 1,000 km of the Sunda megathrust and generated a catastrophic Indian Ocean tsunami. The event caused more than ~230,000 fatalities and remains one of the deadliest earthquakes in recorded history[6–8]. The subsequent March 28, 2005 Nias-Simeulue earthquake (M_w 8.6-8.7) ruptured an adjacent megathrust segment and highlighted along-strike variations in rupture behavior and mechanical characteristics[9–11]. In contrast to these megathrust events, the April 11, 2012 earthquake sequence in the equatorial Indian Ocean consisted of two great intraplate strike-slip earthquakes (M_w 8.6 and M_w 8.2) occurring within the subducting Indo-Australian plate[12–14]. These earthquakes demonstrated active intraplate deformation within the Wharton Basin.

Against this backdrop of major megathrust and intraplate seismicity, numerous studies have attempted to quantify seismic hazard in the Andaman-Nicobar and Sumatra regions. Kataria et al.[15] performed the only dedicated Deterministic Seismic Hazard Analysis (DSHA) for the Andaman-Nicobar Islands. Kolathayar and Sitharam[16] conducted the first regional PSHA for the Andaman-Nicobar Islands using an earthquake catalog up to 2010 and global GMPEs. However, their study employed limited source zonation, equal weighting of GMPEs, and global magnitude homogenization relations, highlighting the need for improved datasets and GMPE selection. Sitharam and Kolathayar[17] later added parts of the Indian region that were close to the PSHA framework. They highlighted the elevated seismic hazard associated with the Andaman subduction interface despite limited offshore seismic data. Mishra et al.[18] represented a major advancement by doing a regional PSHA for the Andaman-Nicobar and Sumatra regions using long term seismicity and extreme value theory. They reported pronounced spatial variability in seismic hazard across the region. Collectively, these studies demonstrate that earlier hazard assessments were constrained by limited offshore data, simplified source representations, and incomplete treatment of epistemic uncertainty. Recent studies have also highlighted the importance of intraplate deformation and complex rupture processes within the Wharton Basin for regional seismic hazard assessment[12,13,19–21]. Recent regional PSHA studies employing logic tree frameworks and statistically weighted GMPEs[22–24] have demonstrated the importance of rigorous uncertainty quantification in hazard assessments for tectonically complex regions. These studies collectively demonstrate the need for updated PSHA frameworks incorporating improved catalog completeness, refined source characterization, and robust uncertainty treatment. These aspects constitute the principal objectives of the present study.

Seismic hazard in tectonically active subduction systems can be evaluated using deterministic and probabilistic approaches[25–27]. Because the Andaman-Sumatra region contains multiple interacting seismic sources with variable recurrence characteristics, PSHA provides a more suitable framework for regional hazard assessment. Despite these advances, existing PSHA studies for the Andaman-Sumatra region remain limited by outdated earthquake catalogs, simplified source zonation, reliance on global magnitude conversions, and equal weight GMPE logic trees that do not adequately represent epistemic uncertainty. Furthermore, intraplate deformation within the Wharton Basin, now recognized as a major contributor to regional seismic hazard, has not been consistently incorporated.

Accordingly, this study presents a comprehensive and updated PSHA for the Andaman-Sumatra subduction zone, integrating an extended homogenized earthquake catalog (1881-2025), multiple declustering schemes, refined source characterization, including intraplate deformation, and statistically weighted GMPEs within a robust logic tree framework.

Study Area and Seismotectonics

The Sumatra-Andaman subduction zone is globally known for its high seismicity and tectonically complex plate boundaries (Fig. 1). The Indo-Australian Plate converges obliquely beneath the Burma-Sunda Plate, resulting in partitioned deformation expressed through megathrust slip along the Sunda subduction interface, strike-slip motion along the Sumatra Fault System, and intraplate deformation within the Wharton Basin[28,29]. This tectonic framework has generated numerous great megathrust and intraplate earthquakes, making the region highly susceptible to severe seismic hazard. This study delineates the Andaman-Sumatra region spatially between 90°E-102°E longitude and 2°N-15°N latitude, including the Andaman-Nicobar Islands, the northern Sumatra segment of the Sunda megathrust, the adjacent forearc and back arc regions, and the intraplate deformation zone of the Wharton Basin. The region hosts multiple seismogenic sources operating at shallow, intermediate, and deep depths. This complex seismotectonic setting makes the region particularly suitable for a comprehensive probabilistic seismic hazard assessment (PSHA).

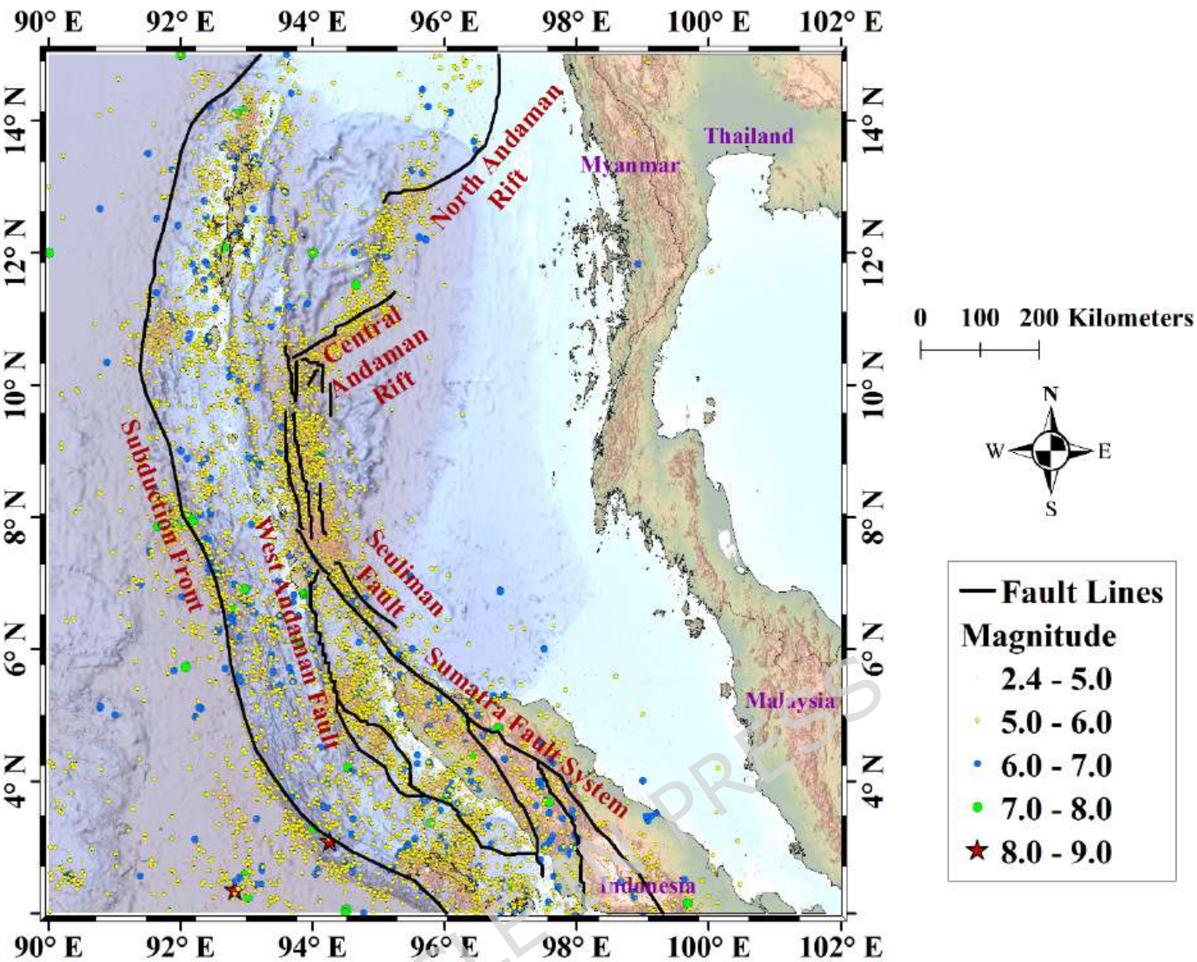

Fig. 1. *Seismotectonic framework of the Andaman-Sumatra subduction zone showing the spatial distribution of earthquake epicenters (M_w 2.4-9.0), major active fault systems, country boundaries, and the Sunda subduction zone. Earthquake epicenters are classified according to magnitude ranges to illustrate regional seismicity patterns and tectonic clustering associated with the Andaman-Sumatra plate boundary system. Major tectonic structures, including the West Andaman Fault, Central Andaman Rift, North Andaman Rift, Sumatra Fault System, and Seuliman Fault are superimposed on shaded bathymetric topographic relief for enhanced tectonic interpretation. Red stars denote great earthquakes ($M_w \geq 8.0$), highlighting the principal seismic sources controlling regional seismic hazard in the study region. Latitude and longitude are shown in decimal degrees, and a uniform scale bar (0-100-200 km) is provided for spatial reference. Map generated by the authors using Esri ArcGIS Desktop 10.8.2 (ArcMap; Esri Inc., Redlands, CA, USA; https://www.esri.com).*

Data and Methodology

Earthquake catalog compilation

Data

A composite earthquake catalog for the Andaman-Sumatra subduction zone is compiled by merging earthquake datasets obtained from multiple agencies, including the United States Geological Survey (USGS), Global Centroid Moment Tensor (GCMT), National Center for Seismology (NCS), International

Seismological Centre (ISC), and Incorporated Research Institutions for Seismology (IRIS). The resulting raw catalog comprises 52,333 events with magnitudes ranging from 1.2 to 9.3, spanning the period 1881-2025 (Table S1). Duplicate events (12,628) are identified and removed based on origin time, hypocentral location, depth, and magnitude, following priority criteria suggested by Tan[30] and Shahabuddin and Mohanty[31], 39,705 unique events remained for subsequent analysis. The decadal distribution of earthquakes by magnitude ≥ 4.0 subset (Table 1) illustrates long term seismicity trends and temporal variations in catalog completeness.

Table 1. *Decadal distribution of earthquakes across different magnitude ranges in the Andaman-Sumatra subduction zone, illustrating long term seismicity trends for earthquakes with* $M_w \geq 4.0$.

Years	**Magnitude Range**											
	4.0-4.49	**4.5-4.99**	**5.0-5.49**	**5.5-5.99**	**6.0-6.49**	**6.5-6.99**	**7.0-7.49**	**7.5-7.99**	**8.0-8.49**	**8.5-8.99**	**9.0-9.5**	**Total**
2021-2025	1412	918	341	111	15	1	1	0	0	0	0	2799
2011-2020	4190	3424	772	203	49	17	4	1	0	1	0	8661
2001-2010	7333	8195	2513	641	198	41	21	8	1	0	1	18952
1991-2000	821	1140	379	93	24	3	1	0	0	0	0	2461
1981-1990	451	1235	505	103	25	8	1	0	0	0	0	2328
1971-1980	72	467	281	71	19	2	2	0	0	0	0	914
1961-1970	0	119	160	46	22	10	1	2	0	0	0	360
1951-1960	0	0	3	39	6	2	1	0	0	0	0	51
1941-1950	0	0	4	30	25	5	0	1	1	0	0	66
1931-1940	0	0	2	53	33	6	1	3	0	0	0	98
1921-1930	0	0	0	27	8	4	1	0	0	0	0	40
1911-1920	0	0	0	5	7	5	2	0	0	0	0	19
1901-1910	0	0	0	1	0	2	0	1	1	0	0	5
1891-1900	0	0	0	0	0	0	0	0	0	0	0	0
1881-1890	0	0	0	0	0	0	0	1	0	0	0	1
Total	14279	15498	4960	1423	431	106	36	17	3	1	1	36755

To select suitable ground motion prediction equations (GMPEs), a dataset of strong motion records is compiled for statistical validation. The dataset comprises station-event pairs with associated moment magnitude (M_w), hypocentral parameters, epicentral distance, and Peak Ground Acceleration (PGA). All waveform records are obtained from the Engineering Strong Motion (ESM) database (https://esm-db.eu, last accessed May 18, 2026), and processed following standardized procedures, including baseline correction and band pass filtering[32]. These processed ground motion records are used for statistical evaluation of selected GMPEs through LLH-based comparison (Table S2).

Homogenisation

To ensure magnitude consistency across the compiled earthquake catalog, the 39,705 distinct events reported in different magnitude scales were homogenized to moment magnitude (M_w). Previous regional hazard studies such as Kolathayar and Sitharam[16], Kataria et al.[15] and Mishra et al.[18] commonly adopted global magnitude conversion relations proposed by Scordilis[33]. In the present study, however, region specific conversion relations developed by Shahabuddin and Mohanty[31] were preferred to better represent the seismotectonic characteristics of the Andaman-Sumatra region.

Reported body wave (m_b), surface wave (M_S), and local magnitude (M_L) values were converted to M_w using regionally calibrated empirical relations. Since m_b, M_S, and M_L exhibit saturation at moderate to large magnitudes, particularly for $M_w > 6.0$, region specific conversion relations were considered more appropriate than generalized global models. The conversion relationships were developed using standard least squares (SR), inverted standard least squares (ISR), and generalized orthogonal regression (GOR) techniques, and the optimal relations were selected based on statistical performance measures including residual distribution, coefficient of determination (R^2), and standard deviation. The adopted relations are provided in Eqs. S1-S11, markedly diminishing magnitude uncertainty and guaranteeing uniformity in ensuing PSHA calculations[31,34–36].

As microearthquakes have relatively high uncertainty and limited influence on regional seismic hazard, events with $M_w < 3$ were excluded from the catalog. Consequently, 2,045 events were removed, resulting in a final homogenized catalog comprising 37,660 earthquakes. A comparison between the regional and global magnitude conversion relations is presented in Table S3, demonstrating the improved consistency and reduced uncertainty achieved through the adoption of region specific magnitude conversion models for the Andaman-Sumatra region. Fig. 2 illustrates the complete methodological framework adopted for the present study.

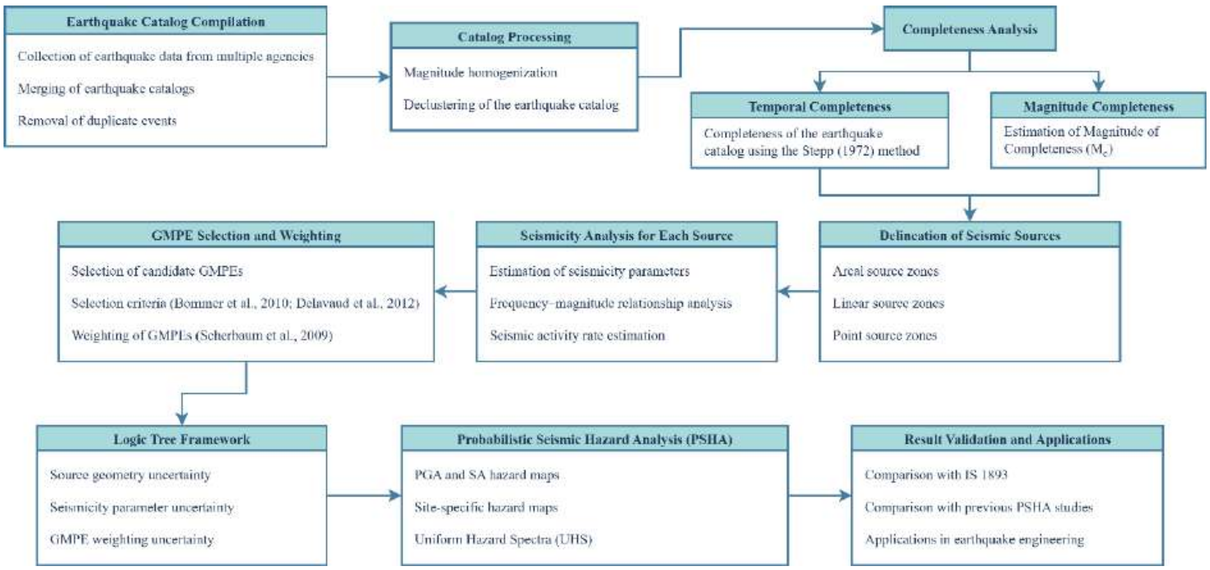

Fig. 2. *Methodological framework of the present study depicting earthquake catalog compilation and processing, catalog completeness assessment, seismic source characterization, treatment of epistemic uncertainties through GMPE selection and logic tree approach, and implementation of PSHA.*

Declustering

Four commonly used declustering methods, namely : Gardner and Knopoff[37], Reasenberg[38], Uhrhammer[39] and Grünthal[40], were evaluated for the compiled earthquake catalog. Since the present study adopts a classical time independent PSHA framework based on the Poisson assumption of earthquake occurrence, declustering was performed to obtain statistically independent background seismicity for recurrence analysis and hazard estimation[16].

The use of declustered catalogs in PSHA remains an active topic of discussion in recent seismological studies. While several studies have suggested that removal of dependent events may influence seismicity characteristics and hazard estimation in clustered or time dependent models[41–44], declustered catalogs continue to be widely used in conventional PSHA applications and National Seismic Hazard Models[45–48].

Declustering was implemented using ZMAP software[40]. The Reasenberg[38] method did not adequately satisfy the Poissonian assumption of temporal independence for the present dataset and was therefore excluded from further analysis. Consequently, Gardner and Knopoff[37], Uhrhammer[39] and Grünthal[40] methods were comparatively evaluated (Table 2).

The Uhrhammer[39], Gardner and Knopoff[37], and Grünthal[40] methods yielded average coefficients of variation (CV) of inter event times of 1.82, 1.54, and 1.47, respectively. Although the Grünthal[40] method produced lower CV values, it also removed a substantially larger number of events, resulting in lower b-values and slightly higher M_c values, suggesting possible over declustering of the catalog. In contrast, the Uhrhammer[39] method retained comparatively stronger clustering characteristics. The Gardner and Knopoff[37] method provided a balanced outcome by preserving the overall seismicity characteristics while maintaining reasonable temporal independence, producing stable b-values, moderate CV values, and consistent magnitude completeness estimates.

Based on this comparative statistical evaluation and consistency with previous regional studies Kolathayar and Sitharam[16], the Gardner and Knopoff[37] declustered catalog was selected for subsequent seismicity analysis and PSHA. The final declustered catalog consists of 10,094 independent earthquake events.

Table 2. *Results of earthquake catalog declustering using different techniques for the Andaman–Sumatra region, showing the proportions of independent and dependent seismic events together with the CV of inter-event times and estimated seismicity parameters (a-value, b-value, and M_c).*

Techniques	Background + Mainshocks	Only Mainshocks	Fore-shocks + after-shocks	Total	Independent Events (%)	Dependent Events (%)	Average CV of Inter-Event Time	b-value	a-value	M_c
Uhrhammer[39]	13072	1155	24588	37660	34.71	65.29	1.82	0.89 ± 0.01	5.739	4.5
Gardner and Knopoff[37]	10094	2128	27566	37660	26.80	73.20	1.54	0.78 ± 0.01	5.150	4.5
Grünthal[40]	6421	1774	31239	37660	17.05	82.95	1.47	0.71 ± 0.01	4.629	4.7

Completeness analysis

The temporal completeness of the earthquake catalog was evaluated using the Stepp[49] method, which examines the variation of seismicity rate standard deviation with increasing observation time under the assumption of Poissonian earthquake occurrence. Deviations from the theoretical $1/\sqrt{T}$ decay trend indicate periods of incomplete earthquake recording. Earthquakes were grouped into four magnitude ranges ($4.0 \leq M < 5.0$, $5.0 \leq M < 6.0$, $6.0 \leq M < 7.0$, and $M \geq 7.0$), and the temporal variation of standard deviation was analyzed for each class (Fig. 3). The catalog was found to be complete for approximately 15-20 years for

4.0 ≤ M < 5.0 events, 20-25 years for 5.0 ≤ M < 6.0, 30-35 years for 6.0 ≤ M < 7.0, and 40-45 years for M ≥ 7.0 earthquakes. The longer completeness periods for larger events reflect their more reliable reporting in historical and early instrumental records. Seismicity parameters used in the PSHA were therefore estimated using only the complete portions of the catalog.

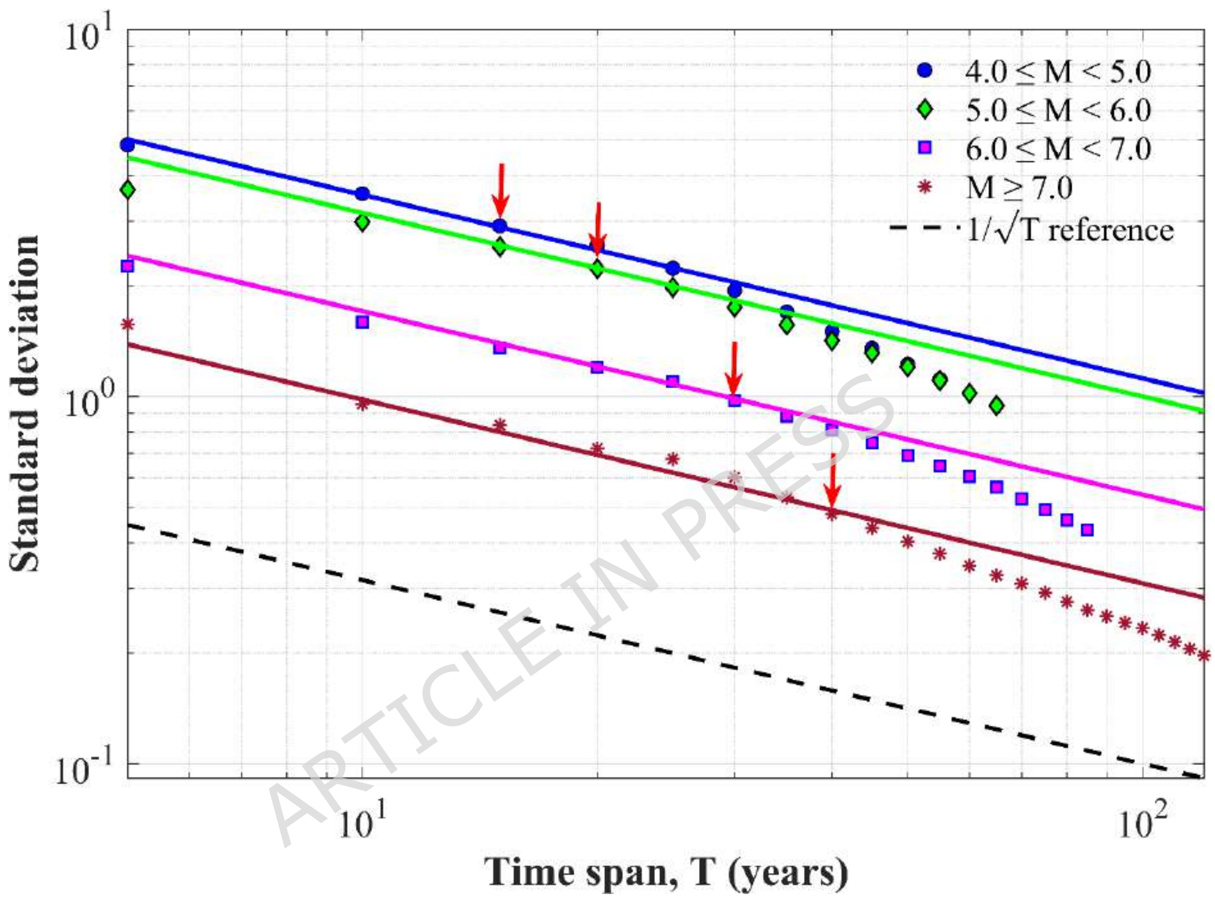

Fig. 3. *Temporal completeness analysis of the earthquake catalog for the Andaman–Sumatra region based on the Stepp[49] method. The figure shows the variation of standard deviation with observation time span (T) for different magnitude ranges (4.0 ≤ M < 5.0, 5.0 ≤ M < 6.0, 6.0 ≤ M < 7.0, and M ≥ 7.0). Colored symbols represent the observed standard deviation for each magnitude interval, while the corresponding solid lines indicate the fitted temporal trend. The black solid line denotes the theoretical 1/√T reference relationship expected for a complete Poissonian earthquake catalog. Red arrows mark the estimated completeness periods for different magnitude classes, indicating the minimum time intervals over which the earthquake catalog can be considered statistically complete for seismic hazard analysis. Figure prepared by the authors using MATLAB R2022b (The MathWorks Inc.; https://www.mathworks.com).*

It is important to distinguish between the temporal completeness of the earthquake catalog and the magnitude of completeness (M_c) used for seismicity parameter estimation. The Stepp[49] method evaluates the temporal stability and robustness of the earthquake catalog by determining the observation periods over which earthquakes of different magnitude ranges are consistently recorded. In contrast, the M_c represents the minimum magnitude above which earthquake occurrence is considered completely recorded for frequency magnitude distribution (FMD) analysis. Therefore, M_c values used for Gutenberg-Richter (GR) seismicity parameter estimation were determined separately using the FMD and the Maximum Curvature (MAXC) method.

Seismic Sources

Seismic source zones are delineated based on the spatial distribution of seismicity, regional tectonic setting, fault geometry, and focal mechanism patterns to capture spatial variability in earthquake occurrence. Each source zone is associated with a zone specific earthquake subset to enable reliable estimation of seismicity parameters such as recurrence rates and magnitude frequency relationships. To represent the complex seismotectonic framework of the study region, three complementary seismic source modeling approaches are adopted: *Areal source zones*, representing distributed seismicity within tectonically coherent regions; *Linear sources*, corresponding to major mapped faults and plate boundary structures; and *Point (gridded) source*, capturing spatial variations in seismicity through kernel based smoothing of the earthquake catalog. The combined use of these source models ensures a comprehensive representation of both fault controlled and diffuse seismicity. This integrated framework better accounts for epistemic uncertainty in the PSHA.

Areal source zones

The study region (2-15°N latitude and 90-102°E longitude) is subdivided into 15 areal seismic source zones based on integrated interpretation of the spatial distribution of homogenized seismicity, regional tectonic framework, mapped fault systems, and similarity in focal mechanism characteristics (Fig. 4). Spatial earthquake clustering and focal mechanism similarity were considered the primary controlling criteria for delineating the source boundaries, while tectonic and structural features were used to maintain regional seismotectonic consistency. In several areas, seismicity patterns did not fully coincide with mapped tectonic boundaries. In such cases, the zonation limits were iteratively refined using earthquake concentration, focal mechanism characteristics, and structural continuity. This approach helped define physically meaningful and relatively homogeneous seismic source zones suitable for PSHA applications. By contrast, Kolathayar and Sitharam[16] delineated a smaller region (90-98°E longitude and 5-18°N latitude) into 11 source zones.

Zones I-III are located west of the Sunda subduction front and represent the outer-rise and forearc domains. These zones are characterized by relatively low to moderate seismicity (N = 74-289) and shallow average focal depths (~17-18 km). Zones I and II exhibit lower activity levels with observed maximum magnitude ($M_{max}^{Obs.}$) of 7.9 and 6.6, respectively, whereas Zone III shows comparatively higher seismicity ($\lambda = 3.51 \pm 2.17$) and the $M_{max}^{Obs.} = 8.6$ with dominant strike-slip faulting mechanisms (Table 3). Based on the focal mechanism solutions (Table 3), these zones are predominantly characterized by normal and strike-slip faulting, with localized occurrences of thrust mechanisms.

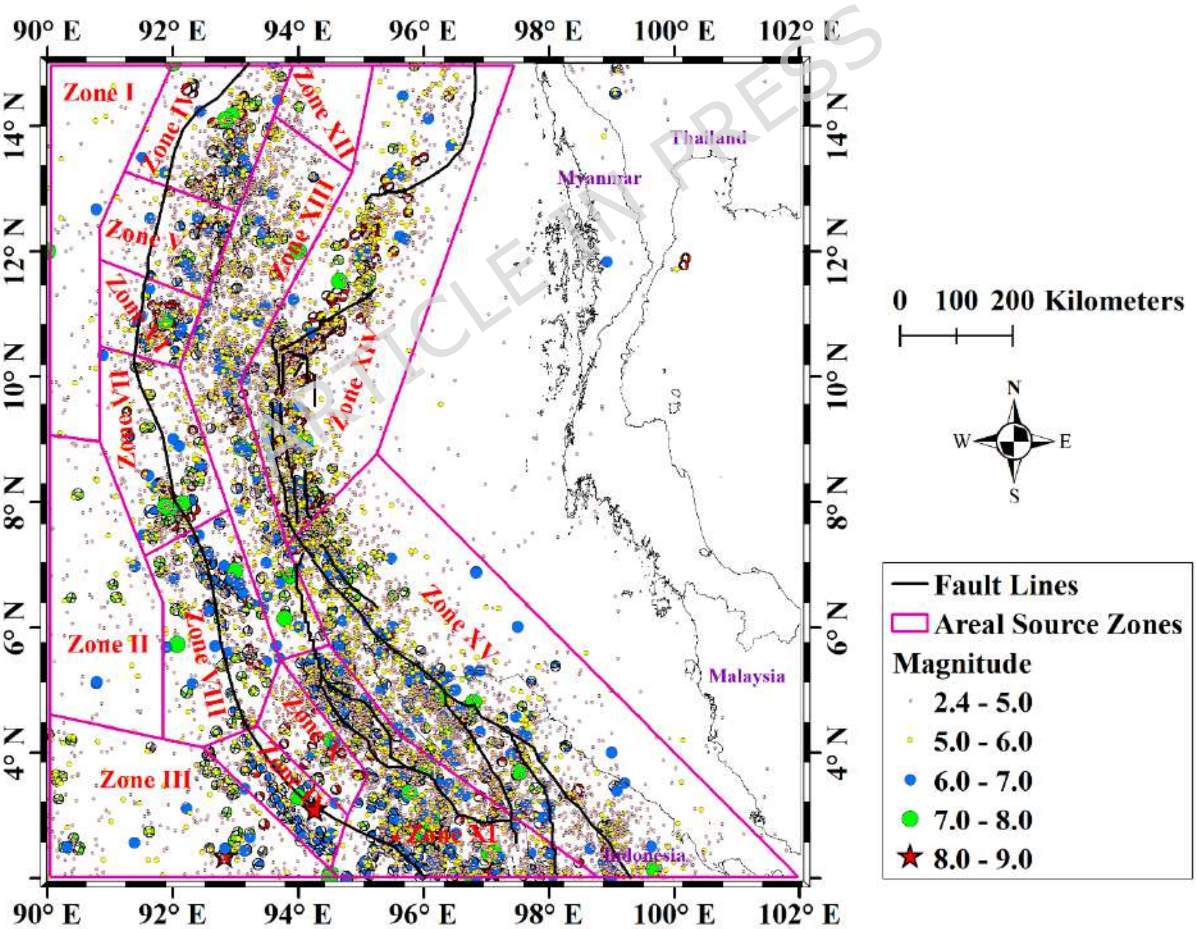

Fig. 4. *Delineated areal seismic source zones of the Andaman-Sumatra subduction zone showing the spatial distribution of earthquake epicenters (Mw 2.4-9.0), mapped active fault systems, focal mechanism solutions, and tectonic framework considered for PSHA). The study region was subdivided into fifteen areal seismic source zones based on integrated analysis of spatial seismicity patterns, regional tectonic configuration, mapped fault geometries, and focal mechanism characteristics. The delineated*

source boundaries were designed to represent relatively homogeneous seismotectonic domains exhibiting similar seismic behavior and faulting characteristics. Magenta polygons represent the adopted areal seismic source zones, while black lines denote major active tectonic structures associated with the study area. Latitude and longitude are shown in decimal degrees, and a uniform scale bar (0-100-200 km) is provided for spatial reference. Map generated by the authors using Esri ArcGIS Desktop 10.8.2 (ArcMap; Esri Inc., Redlands, CA, USA; https://www.esri.com).

The subduction interface and associated forearc regions are represented by Zones IV-XI, which collectively account for the highest concentration of seismicity in the study area. These zones display diverse faulting styles, including reverse, normal, and strike-slip mechanisms, reflecting complex strain partitioning along the obliquely convergent Indo-Australian and Burma-Sunda Plate boundary. Zones IV-X exhibit moderate to high seismic activity (N = 176-467), with b-values ranging from 0.72 to 0.87 and $M_{max}^{Obs.}$ up to 9.0 (Zone IX). Zone XI, encompassing the deeper segment of the West Andaman Fault system, is distinguished by a large number of events (N = 1,722), greater average focal depths (~38 km), and a high seismicity rate (λ = 9.78 ± 1.96), indicating significant seismogenic potential. Zones XII and XIII are situated between the subduction front and major regional fault systems, including the North Andaman Rift, Central Andaman Fault, West Andaman Fault, and the Sumatra Fault System. Zone XII is characterized by sparse seismicity (N = 61), a high b-value (1.41 ± 0.19), and a relatively low $M_{max}^{Obs.} = 5.6$, whereas Zone XIII exhibits substantially higher activity (N = 1,550) with deeper average focal depths (~44 km) and elevated seismicity rates (λ = 8.79 ± 1.85). Zones XIV and XV correspond to major strike-slip dominated fault systems, including the Andaman Rift, Central Andaman Fault, and the Sumatra Fault System. These zones record the highest number of earthquakes (N = 1,554-2,563) and the largest seismicity rates (λ up to 14.5 ± 2.9), reflecting intense deformation along major intracontinental and plate boundary faults. The predominance of strike-slip faulting in Zone XV is consistent with the kinematics of the Sumatra Fault System and its role in accommodating oblique plate convergence.

Linear source zones

Fig. 5 represents the linear seismic sources situated along major active faults and plate boundary structures in the study region. The entire region is segmented into 15 linear source zones (listed in Table 4) for all faults. Each linear source zone is defined by buffering the mapped fault trace by 20 km on either side to account for location uncertainty and off-fault seismicity. The principal faults include the Sunda subduction front, Central Andaman Rift, West Andaman Fault, Seuliman Fault, North Andaman Rift, and the Sumatra Fault System, and nine additional minor fault segments designated as Fault 1-9. These structures exhibit varying orientations, predominantly trending NW-SE to NNW-SSE parallel to the Sunda trench, while several intra-arc faults show N-S to NE-SW alignments. The fault systems are characterized by diverse kinematics, including normal faulting associated with back-arc extension, reverse faulting related to compressional deformation along the plate boundary, and strike-slip motion along major intracontinental structures such as the Sumatra Fault System and Central Andaman Rift. The mapped faults extend for several tens to hundreds of kilometres and have generated significant historical and instrumental earthquakes, including several events exceeding magnitude 7, highlighting their major contribution to the regional seismic hazard. The geometric and seismotectonic parameters of the identified linear sources, including fault type, seismicity statistics, and $M_{max}^{Obs.}$, are summarized in Table 4. The linear fault-source model was not intended to exclusively represent the complete regional seismicity. Earthquakes occurring outside mapped linear fault zones are incorporated through the alternative areal and point source representations within the logic tree framework, thereby accounting for distributed background seismicity and minimizing possible underestimation of seismic hazard.

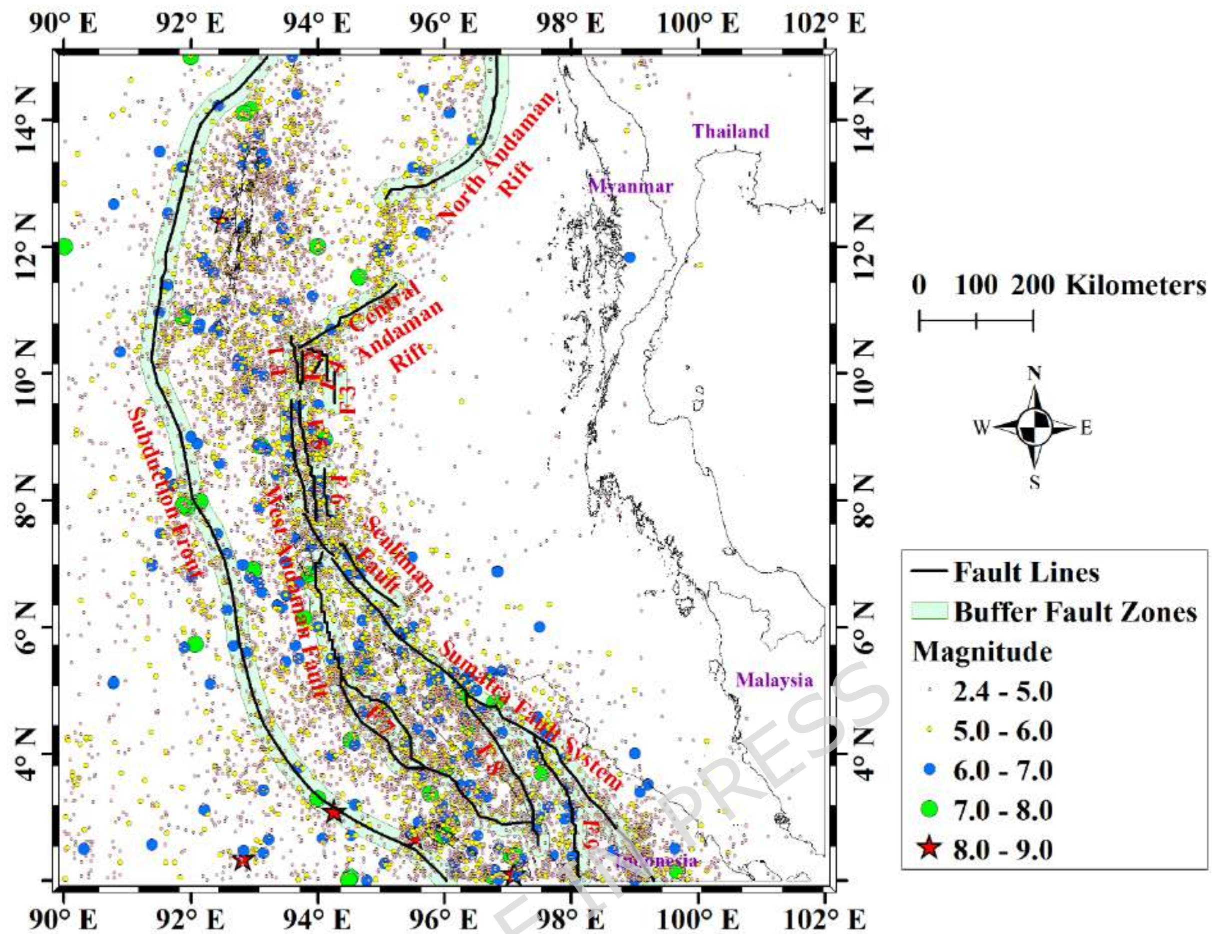

Fig. 5. *Delineation of 15 linear seismic source zones along the major active tectonic structures of the Andaman-Sumatra subduction zone based on mapped fault traces, regional tectonic framework, and the spatial distribution of homogenized earthquake epicenters. Black lines represent the Sunda subduction front and major active fault systems, while the light green shaded regions denote the 20 km buffered fault zones considered for seismic source characterization and seismicity association. Fault geometries and tectonic lineaments were adopted from Cattin et al.*[50]*. Earthquake epicenters are classified according to moment magnitude ranges (2.4-5.0, 5.0-6.0, 6.0-7.0, 7.0-8.0, and 8.0-9.0), with red stars indicating great earthquakes (Mw ≥ 8.0). The figure highlights the principal seismogenic structures of the region, including the Sunda subduction front, Central Andaman Rift, North Andaman Rift, West Andaman Fault, Seuliman Fault, and Sumatra Fault System, together with nine additional minor fault segments labelled F1–F9 in the figure for clarity of visualization. Country boundaries and coastlines of Myanmar, Thailand, Malaysia, and Indonesia are included to provide regional geographic context. Latitude and longitude are shown in decimal degrees, and a uniform scale bar (0-100-200 km) is provided for spatial reference. Map generated by the authors using Esri ArcGIS Desktop 10.8.2 (ArcMap; Esri Inc., Redlands, CA, USA; https://www.esri.com).*

Point source zones

During the delineation of areal and linear seismic sources, a substantial degree of spatial scatter is observed in the earthquake distribution. Many events are not clearly linked to any mapped fault or source zone. This introduces subjectivity into the definition of discrete seismic sources, particularly in tectonically complex regions such as the Andaman-Sumatra subduction zone. To address this limitation, a zoneless or gridded seismicity methodology named Point source is implemented, enabling the modelling of seismic hazards without dependence on explicitly delineated fault geometries. The zoneless methodology, initially proposed by Frankel[51] and subsequently refined by Woo[52] relies on direct estimation of spatial variations in seismic activity rates from the earthquake catalog. This method has been used a lot in places where seismic sources are spread out or not well defined[16,53–58].

In this approach, the study area was subdivided into regular 0.1° × 0.1° spatial grids, resulting in 15,600 grid nodes across the study region. Since many individual grid cells contain insufficient earthquake events for statistically stable estimation of source-wise M_c values, a uniform M_c value of M_w 4.5 derived from the regional FMD analysis (Fig. S3) was adopted for the gridded seismicity calculations.

Recurrence rates were estimated at each grid node and spatially smoothed using a Gaussian kernel following Woo[52]. The mean annual seismic activity rate density λ[52] for magnitude M at location x is expressed as:

$$\lambda(M,x) = \sum_{i=1}^{N} \frac{K(M, x - x_i)}{T(x_i)} \tag{1}$$

Where $\lambda(M,x)$ is expected annual number of earthquake of magnitude M occurring at location x_i , N is total number of earthquakes in the catalog for magnitude $M \geq M_c$, x_i is the epicentral location of the i^{th} earthquake, $T(x_i)$ is the effective observation time (catalog completeness period) for i^{th} event and K $(M, x - x_i)$ is the magnitude dependent spatial kernel function[52], given by

$$K(M,r) = \frac{(a-1)}{\pi} h(M)^{-2} \left[1 + \left(\frac{r}{h(M)}\right)^2\right]^{-a} \tag{2}$$

Where $r = |x - x_i|$ and $h(M)$ is the magnitude dependent bandwidth, given by $h(M) = He^{kM}$, where H and k are region specific constant.

The spatial distribution of smoothed seismicity is shown in Fig. 6. Elevated λ values (0.0957-0.1670) are concentrated along the subduction margin, particularly along the subduction front, west Andaman fault, Sumatra fault system, Seuliman fault, and the central Andaman Rift, compared to the surrounding regions. Seven key locations were additionally identified and annotated in Fig. 6, namely Radhanagar Beach, Port Blair, Neil Island, Car Nicobar, Indira Point, Banda Aceh, and Meulaboh (West Aceh). These sites were selected to represent major population centers, strategically important islands, and regions exhibiting varying proximity to the Sunda megathrust and associated subduction related tectonic features. The selected locations were further utilized for detailed seismic hazard analysis and site specific hazard evaluation.

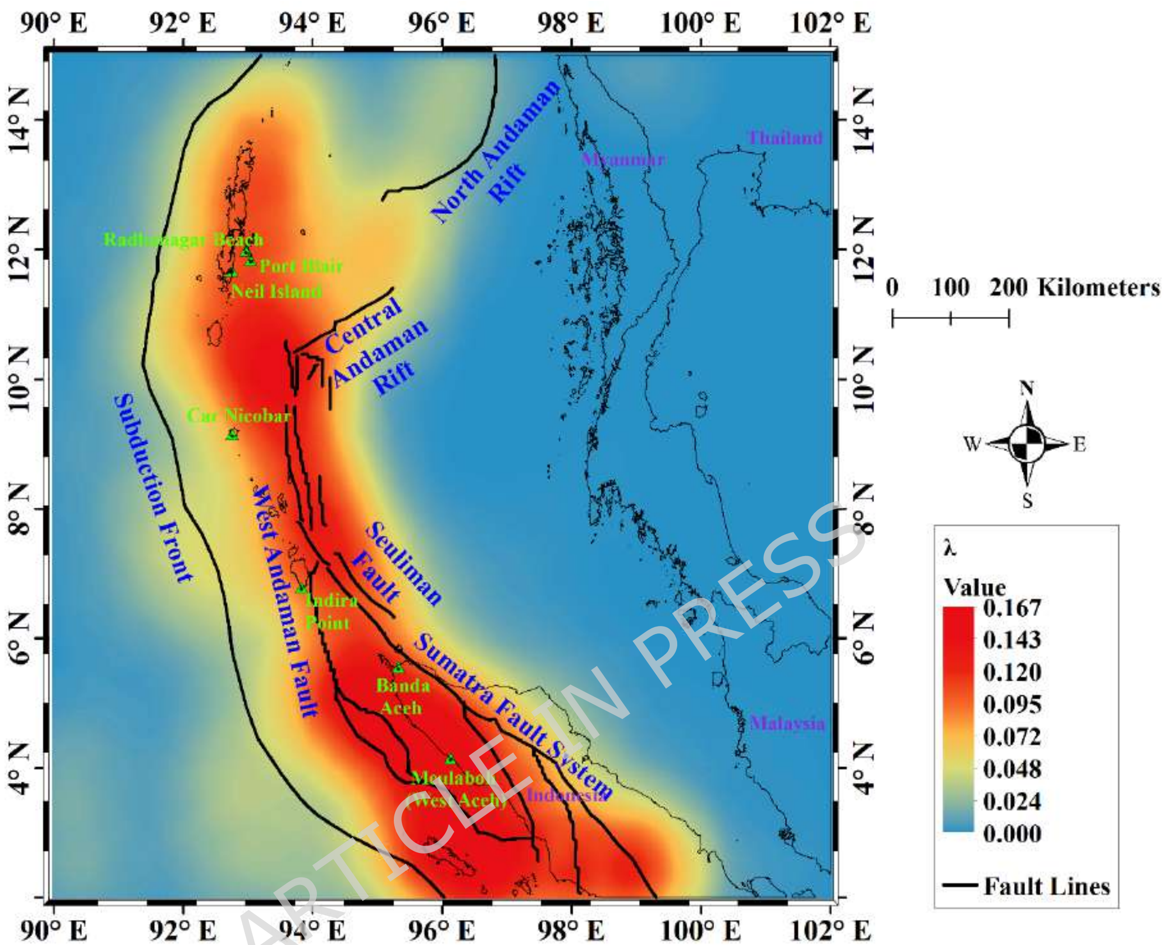

Fig. 6. *Spatial distribution of the seismic activity rate (λ-value) for the gridded point-source seismicity model of the Andaman-Sumatra region, computed on a 0.1° × 0.1° latitude-longitude grid using the homogenized and declustered earthquake catalog. The color gradient represents the annual seismicity rate (λ), where warmer colors (red to orange) indicate regions of higher earthquake occurrence and cooler colors indicate relatively lower seismic activity. Elevated λ-values are predominantly concentrated along the Sunda Subduction Front, West Andaman Fault, Central Andaman Rift, Seuliman Fault, and the Sumatra Fault System, reflecting intense tectonic activity associated with the Andaman-Sumatra subduction zone. Major mapped fault traces are shown by black solid lines, while important tectonic segments and islands including North Andaman Rift, Car Nicobar, Indira Point, Banda Aceh, and the Mentawai region are annotated for reference. The green triangles represent the key selected locations. Country boundaries and coastlines of Myanmar, Thailand, Malaysia, and Indonesia are included to provide regional geographic context. Latitude and longitude are shown in decimal degrees, and a uniform scale bar (0-100-200 km) is provided for spatial reference. Map generated by the authors using Esri ArcGIS Desktop 10.8.2 (ArcMap; Esri Inc., Redlands, CA, USA; https://www.esri.com).*

Seismicity Analysis

The seismic activity of the study region is characterized using the GR earthquake recurrence relationship[59].

In the present study, the seismicity parameters for each source are estimated individually using the maximum likelihood method (MLM), which provides statistically robust estimates and avoids biases associated with magnitude binning of earthquake data[60,61]. The analysis explicitly considers the M_c, defined as the lowest magnitude above which the earthquake catalog can be regarded as complete[62,63]. Only earthquakes with $M_w \geq M_c$ were considered for recurrence analysis to ensure reliable estimation of seismicity parameters. In addition to the classical b-value, the exponential form of the FMD, represented by the β-value, is computed as $\beta = b\ln(10)$. The seismic activity rate (λ), representing the mean annual rate of earthquakes exceeding the completeness magnitude, is also estimated for each seismic source and is given by $\lambda = 10^{(a-bM_c)}$[25,26,64].

The seismicity parameters for each areal source are estimated independently and given in Table 3 and plotted in Fig. S1. The estimated b-values across the areal seismic source zones generally range between 0.6 and 0.9 (Table 3) , which is consistent with values reported for active subduction and strike-slip tectonic environments[65–67]. Lower b-values observed in several subduction interface and major fault zones indicate a relatively higher proportion of large magnitude earthquakes, reflecting elevated stress accumulation along these structures. Among the areal source zones, Zones III, V, IX, XI, XIII, XIV, and XV exhibit relatively high λ and large $M_{max}^{Obs.}$, highlighting their dominant contribution to regional seismic hazard. In particular, Zones V and IX show $M_{max}^{Obs.}$ approaching M_w 8.4 and 9.0 respectively, emphasizing the potential for great earthquakes along the subduction interface and adjacent forearc regions. Zone XI, characterized by greater average focal depths and high seismicity rates, reflects seismic deformation within the deeper portion of the subduction interface. In contrast, Zones XIV and XV, associated with major strike-slip fault systems, exhibit high earthquake counts and activity rates, indicating intense crustal deformation related to oblique plate convergence and lateral strain partitioning.

Table 3. *Earthquake hazard parameters estimated independently for each areal seismic source zone using the Kijko-Sellevoll-Bayes method*[68,69]*. Here, σb, σβ and σλ denote the standard deviations of the b value, β value and λ, respectively. FT denotes fault type: N-normal faulting, R-reverse faulting, SS-strike-slip faulting, and U-undefined. ATSCR refers to the Active Tectonic Shallow Crustal Region, and SIR denotes the Subduction Interface Region.*

Areal Source Zone	FT	N	M_c	Average depth (Km)	M_{min}	$N \geq M_c$	b±σb	a value	β ± σβ = (b·ln(10))	λ ± σλ	$M_{max}^{Obs.}$	Remarks
Zone I	U	74	4.1	17.16	3.5	67	0.73 ± 0.09	2.7	1.68 ± 0.21	0.47 ± 0.40	7.9	ATSCR
Zone II	U	114	4.3	17.42	3.9	80	0.69 ± 0.06	2.9	1.59 ± 0.14	0.91 ± 0.54	6.6	ATSCR
Zone III	SS	289	4.5	17.73	3.5	185	0.83 ± 0.06	4.3	1.91 ± 0.14	3.51 ± 2.17	8.6	ATSCR

Zone IV	SS	460	4.5	22.46	3.4	279	0.80 ± 0.04	3.9	1.84 ± 0.09	2.21 ± 0.90	7.5	ATSCR
Zone V	N	176	4.7	15.89	3.8	63	0.87± 0.08	4.2	2.00 ± 0.18	1.16 ± 1.01	8.4	ATSCR
Zone VI	R	213	4.4	15.66	3.5	136	0.73 ± 0.05	3.4	1.68 ± 0.12	1.40 ± 0.71	7.9	ATSCR
Zone VII	SS	347	4.4	19.04	3.7	207	0.78 ± 0.05	3.7	1.80 ± 0.12	2.00 ± 1.01	7.5	ATSCR
Zone VIII	N	467	4.3	19.71	3.7	325	0.72 ± 0.04	3.5	1.66 ± 0.09	2.69 ± 1.08	7.4	ATSCR
Zone IX	N	290	4.1	16.94	2.8	265	0.63 ± 0.05	3.1	1.45 ± 0.12	3.64 ± 1.69	9.0	ATSCR
Zone X	R	244	4.1	18.71	3.9	229	0.77 ± 0.05	3.5	1.77 ± 0.12	2.37 ± 1.13	7.1	ATSCR
Zone XI	N	1722	4.4	38.02	3.2	1177	0.74 ± 0.02	4.2	1.70 ± 0.05	9.78 ± 1.96	8.3	SIR
Zone XII	U	61	4.6	33.35	3.3	29	1.41 ± 0.19	6.2	3.25 ± 0.44	0.58 ± 1.17	5.6	ATSCR
Zone XIII	N	1550	4.5	44.39	2.8	956	0.83 ± 0.02	4.7	1.91 ± 0.05	8.79 ± 1.85	7.2	SIR
Zone XIV	R	1554	4.5	31.62	2.4	1122	0.78 ± 0.02	4.5	1.80 ± 0.05	9.65 ± 2.03	7.5	SIR
Zone XV	SS	2563	4.4	71.35	3.1	2312	0.72 ± 0.02	4.35	1.66 ± 0.05	14.50 ± 2.90	7.9	SIR

Earthquake hazard parameters for each linear seismic source were estimated using the Kijko-Sellevoll-Bayes method[68,69] approach considering source specific earthquake catalogs and completeness characteristics. The M_c for each of the 15 linear seismic source zones was independently estimated using the FMD and MAXC method, and given in Table 4 and plotted in Fig. S2. Furthermore, two weighting parameters, η_i *and* μ_i, are estimated for each linear source to account for the relative contribution of fault associated seismicity and fault geometry. The parameter η_i represents the proportion of earthquakes associated with a given linear source relative to the total number of earthquakes in the region, while μ_i represents the normalized contribution of fault length. These parameters are expressed as:

$$\eta_i = \frac{Number\ of\ events\ associated\ with\ the\ source}{total\ number\ of\ the\ events\ in\ the\ region} \tag{3}$$

$$\mu_i = \frac{L_i}{\sum L_i} \tag{4}$$

where, L_i is the length of the ith fault and $\sum L_i$ is the cumulative length of all faults within the corresponding areal seismic source. For linear seismic sources, the weighting parameters η_i and μ_i indicate that the Subduction Front, West Andaman Fault, and Sumatra Fault System contribute disproportionately to regional seismicity, owing to their greater fault lengths and higher concentration of associated earthquakes. These results highlight the critical role of major plate boundary and intracontinental faults in controlling seismic hazard within the study region.

Table 4. *Earthquake hazard parameters estimated for each Linear seismic sources using the Kijko-Sellevoll-Bayes[68,69]. Here σb, σβ and σλ are the standard deviation of b value, β value and mean seismic activity rate(λ). FT denotes fault type: N-normal faulting, R-reverse faulting, SS-strike-slip faulting, and U-undefined.*

	Linear Sources	**FT**	**N**	**M_c**	**Average depth (Km)**	**M_{min}**	**N≥ M_c**	**b±σb**	**a value**	**β ± σβ = (b·ln(10))**	**λ ± σλ**	**$M_{max}^{Obs.}$**	**η**	**μ**
1	Subduction Front	N	495	4.8	19.52	3.6	147	0.72±0.06	3.6	1.66 ± 0.14	0.47 ± 0.32	9.0	0.05	0.294
2	Central Andaman Fault	R	176	5.1	30.00	3.7	40	1.24±0.14	6.2	2.85 ± 0.32	0.18 ± 0.29	6.3	0.02	0.036
3	West Andaman Fault	N	972	4.4	38.23	3.4	702	0.73±0.02	4.0	1.68 ± 0.05	3.07 ± 0.60	7.4	0.10	0.180
4	Fault 7	N	309	4.5	36.03	3.6	201	0.95±0.05	4.7	2.19 ± 0.12	1.62 ± 0.84	6.6	0.03	0.044
5	Seuliman Fault	SS	134	4.7	64.26	3.5	76	0.69±0.06	3.3	1.59 ± 0.14	0.70 ± 0.49	6.6	0.01	0.026
6	Fault 1	R	158	4.6	50.02	3.8	88	1.21±0.10	5.7	2.79 ± 0.23	0.47 ± 0.49	5.8	0.02	0.017
7	Fault 2	R	123	4.6	42.97	4.0	69	1.19±0.10	5.6	2.74 ± 0.23	0.39 ± 0.41	5.7	0.01	0.010
8	Fault 3	R	110	4.5	35.85	3.6	75	0.88±0.07	4.0	2.03 ± 0.16	0.85 ± 0.52	5.9	0.01	0.025
9	Fault 4	R	54	4.6	35.97	4.0	28	0.97±0.12	4.1	2.23 ± 0.28	0.39 ± 0.48	5.5	0.01	0.005
10	Fault 5	R	224	4.4	33.59	3.5	194	0.67±0.04	3.2	1.54 ± 0.09	2.45 ± 1.05	6.4	0.02	0.039
11	Fault 6	R	113	4.6	32.47	3.5	71	0.71±0.07	3.2	1.64 ± 0.16	0.82 ± 0.59	6.5	0.01	0.015
12	Fault 8	SS	371	4.4	47.56	3.5	220	0.78±0.05	3.2	1.80 ± 0.12	2.01 ± 1.01	7.3	0.04	0.054
13	Fault 9	SS	205	4.0	69.50	3.8	199	0.57±0.03	2.5	1.31 ± 0.07	3.74 ± 1.36	7.7	0.02	0.049
14	North Andaman Rift	U	74	4.3	20.51	2.4	51	0.79±0.09	3.1	1.82 ± 0.21	0.90 ± 0.80	6.7	0.01	0.062
15	Sumatra Fault System	SS	615	4.2	82.50	3.5	499	0.60±0.02	3.1	1.38 ± 0.05	3.46 ± 0.70	7.3	0.06	0.142

The spatial distribution of seismicity parameters estimated for the Point source model is shown in Fig. 7. Lower b-values along the Sunda megathrust and major strike-slip fault systems indicate elevated stress accumulation and greater likelihood of large earthquakes, whereas relatively higher b-values in diffuse deformation regions suggest more heterogeneous stress conditions (Fig. 7a). Similar spatial trends are observed for the corresponding β-values (Fig. 7b). The spatial distribution of $M_{max}^{Obs.}$ shows higher values concentrated along the Sunda megathrust and the southern Sumatra segment, reflecting the potential for great earthquakes along the plate boundary, while comparatively lower values are observed away from the active subduction interface and within intraplate domains (Fig. 7c). Together, these spatial patterns highlight the strong influence of tectonic setting, stress regime, and fault architecture on the seismicity characteristics of the study area.

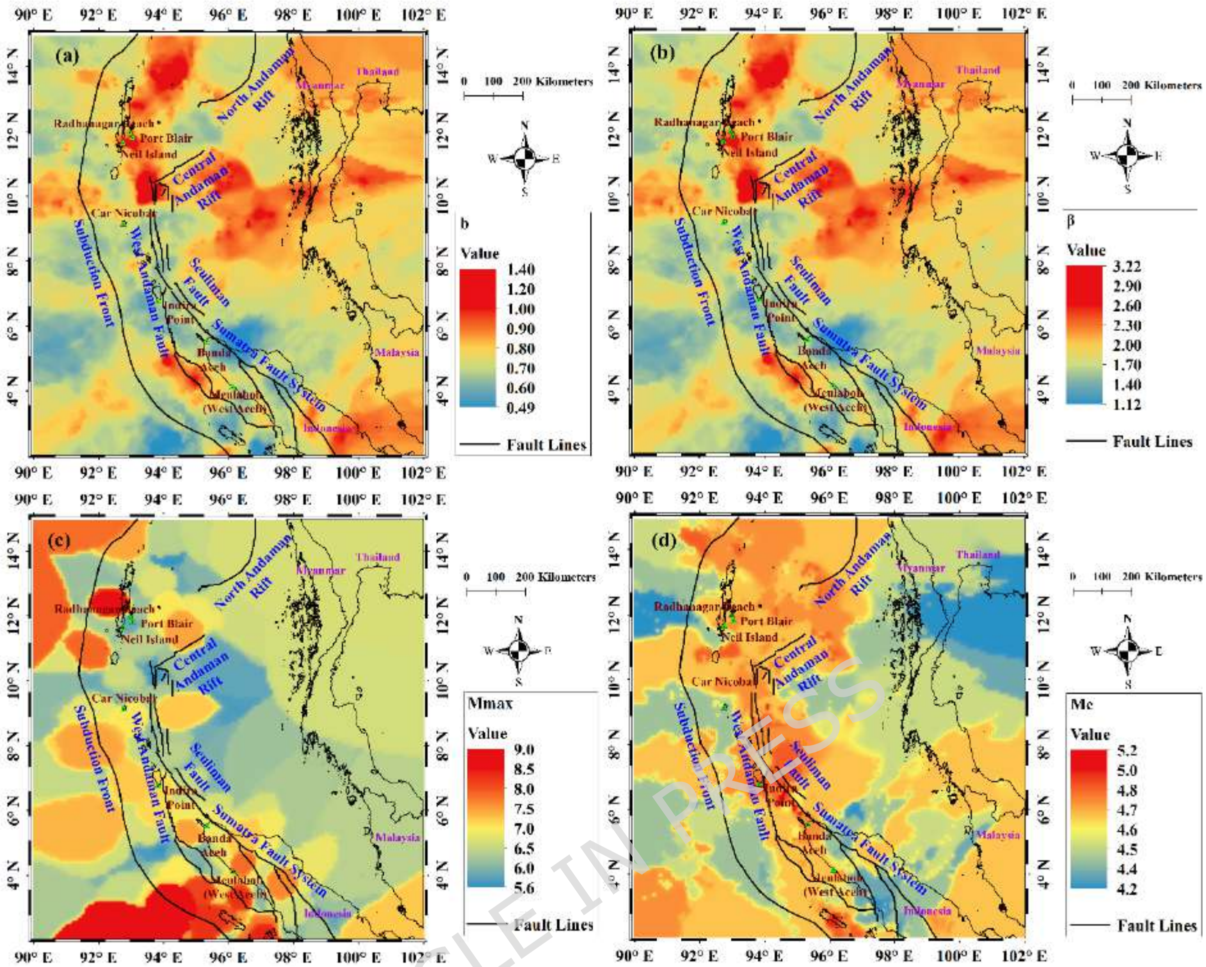

Fig. 7. *Spatial distribution of seismicity parameters across the Andaman-Sumatra region estimated on a 0.1° × 0.1° grid. (a) Spatial variation of the b-value, estimated using the MLM method, showing significant heterogeneity related to variations in stress regime and tectonic setting. (b) Spatial distribution of the corresponding β-values derived from the GR relationship. (c) Spatial distribution of the* $M_{max}^{Obs.}$, *highlighting higher values along the Sunda megathrust and southern Sumatra segment, indicative of the potential for great earthquakes along the plate boundary. (d) Spatial distribution of the* M_c *value, illustrating variations in earthquake detection capability across the region, with generally higher* M_c *values in offshore and deep-water areas due to limited seismic network coverage. Map generated by the authors using Esri ArcGIS Desktop 10.8.2 (ArcMap; Esri Inc., Redlands, CA, USA; https://www.esri.com).*

The FMD considering all events for point source model is plotted in Fig. S3 and illustrated that M_c is 4.5. The spatial variability of the M_c at each node, Fig. 7d, reflects differences in seismic network coverage and earthquake detectability across the region. Higher M_c values in offshore and deep water regions underscore the importance of accounting for spatially varying completeness thresholds to avoid underestimation of seismicity rates in probabilistic hazard assessments.

The selection of appropriate ground motion prediction equations (GMPEs) is a critical component of PSHA, as hazard estimates are highly sensitive to the adopted ground motion models. Consequently, a systematic and transparent GMPE selection procedure is essential for obtaining robust hazard estimates. Based on a comprehensive literature review, eleven candidate GMPEs applicable to tectonic environments similar to the Andaman-Nicobar and Sumatra regions are initially considered. These models are screened using the selection criteria proposed by Bommer et al.[70] and Delavaud et al.[71], accounting for tectonic relevance, magnitude and distance applicability, dataset quality, functional form, and publication status. GMPEs failing to satisfy these criteria are excluded, with reasons documented in Table S4. The performance of the shortlisted GMPEs is quantitatively evaluated using the log-likelihood (LLH) method of Scherbaum et al.[72] which assesses the agreement between observed and predicted ground motions. The LLH calculation requires processed strong motion waveform records with reliable observations of PGA. A total of 16 earthquake events comprising three-component strong motion waveform recordings (48 recordings in total) were selected for the LLH analysis (Table S2). The corresponding waveform records are obtained from the ESM database (https://esm-db.eu/#/station/GE/LHMI (last accessed May 18, 2026)) and processed following standardized procedures described by Pacor et al.[32]. The LLH metric provides a robust statistical measure of the agreement between GMPE predicted ground motions and observed data within the study region. The resulting LLH values, together with the derived likelihood weights and the Data Support Index (DSI), are presented in Table 5 and form the basis for objective selection and weighting of GMPEs in the present PSHA, Eqs. 5-6.

$$w_j = \frac{2^{-LLH}}{\sum_i^n 2^{-LLH_i}} \tag{5}$$

$$DSI = \frac{\left(w_j - \frac{1}{M_c}\right) \times 100}{\frac{1}{M_c}} \tag{6}$$

Where, n is the total no. of GMPEs taken for checking of selection criteria.

Based on statistical performance and tectonic compatibility, four GMPEs are retained for the final logic-tree framework (Table 5). The selected models provide complementary coverage of subduction and shallow crustal ground motion behavior and collectively capture epistemic uncertainty in ground motion prediction for the Andaman-Sumatra region.

Table 5. *Final selection and statistical ranking of the adopted GMPEs for the Andaman-Sumatra region based on LLH analysis. The table summarizes the selected GMPEs together with their applicable SPR range, distance metric, magnitude range, LLH values, normalized weighting factors (wi), and DSI values used in the PSHA logic tree framework. Lower LLH values indicate better agreement between observed and predicted ground motion parameters.*

SN	Selected GMPEs	SPR (sec)	Distance metric (typical)	M range	LLH	2^{-LLH}	w_j	DSI
1	Lin and Lee[73]	0.00-5.00	15-630	5.3-8.1	2.56	0.169576	0.778253	250.2138
2	Zhao et al.[74]	0.05-5.00	<120	5.0-8.0	4.43	0.046391	0.212909	-4.19081
3	Akkar and Bommer[75]	0.00-3.00	<100	5-7.6	9.10	0.001822	0.008363	-96.2365
4	Youngs et al.[76]	0.00-3.00	10-500	>5	13.24	0.000103	0.000474	-99.7865

Logic Tree

A logic tree framework was adopted to explicitly account for epistemic uncertainties associated with seismic source characterization, seismicity parameters, maximum possible earthquake magnitude (M_{max}), and ground motion prediction in the PSHA. This methodology was first formally introduced in seismic hazard analysis by Kulkarni et al.[77] and has since been widely adopted in regional and national PSHA studies worldwide[22–24,78–81]. In the present study, the logic tree comprises four hierarchical branching levels: (i) seismic source type, (ii) β-value, (iii) M_{max}, and (iv) GMPEs, as shown in Fig. 8. At the first branching level, three alternative seismic source representations areal, linear, and point source models, were considered to capture variability in source geometry and seismicity distribution. Each source representation was evaluated independently within the logic tree framework. Hazard contributions were combined probabilistically through branch weighting, thereby minimizing the possibility of double counting seismicity. Branch weights of 0.33, 0.34, and 0.33 were assigned to the areal, linear, and point source models, respectively, reflecting the absence of definitive evidence favoring any single source representation. At the second branching level, uncertainty in seismicity parameters is incorporated using three alternative β-values (β - σβ, β, and β + σβ). The corresponding branch weights are assigned as 0.33, 0.34, and 0.33, respectively, giving slightly greater preference to the mean seismicity model while accounting for statistical variability in the GR relationship. At the third branching level, epistemic uncertainty associated with the M_{max} is incorporated through two alternative upper bound magnitude branches, M_{max} and M_{max} + 0.5, following the recommendation of Kijko[69]. The M_{max} values were estimated using the Kijko-Sellevoll statistical approach[69], in which the M_{max} is derived as a function of the $M_{max}^{obs.}$, earthquake recurrence characteristics, and catalog completeness. Accordingly, the estimated M_{max} values are always greater than the largest historically $M_{max}^{obs.}$ and therefore account for the possibility of future larger events beyond the available seismic record. An additional branch of M_{max} + 0.5 was considered to incorporate epistemic uncertainty associated with the estimation of upper bound earthquake magnitudes in the study area. Equal weights were assigned to both branches due to limited geological and paleoseismological constraints on the absolute upper magnitude limits of the regional seismic sources. At the final level, ground motion uncertainty is represented using four GMPEs suitable for subduction and active tectonic environments[73–76]. These models are weighted according to their relative statistical performance derived from the LLH analysis, with weights of 0.7782, 0.2119, 0.0084 and 0.0005 respectively. In addition to epistemic uncertainty represented through the logic tree framework, aleatory variability is incorporated through the logarithmic standard deviation (σ) terms associated with the selected GMPEs. The adopted GMPEs employ total sigma formulations, which inherently account for both inter-event and intra-event ground motion variability. During GMPE evaluation, the published sigma values of each model are directly incorporated into the probability density calculations and negative average log-likelihood (LLH) analysis used for model selection and weighting. Separate decomposition of aleatory variability into individual components is not implemented, as the selected GMPEs are applied in their original published functional forms. This treatment is consistent with standard regional PSHA practice and adequately captures the natural randomness associated with earthquake ground motion prediction. The combination of three source models, three β-value alternatives, two M_{max} branches, and four GMPEs results in a total of 72 logic tree branches (3×3×2×4), allowing systematic propagation of epistemic uncertainties into the final seismic hazard estimates.

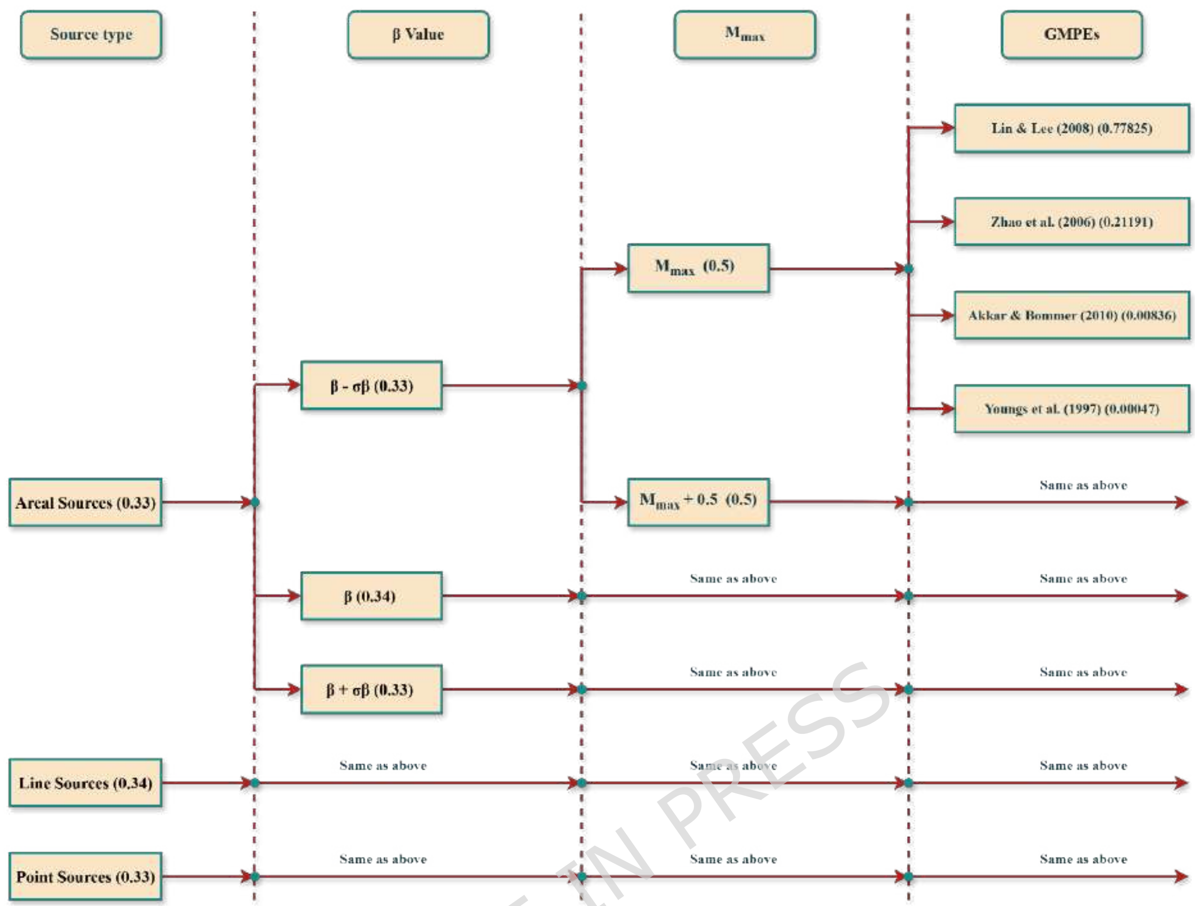

Fig. 8. *Logic tree framework adopted in the present PSHA to incorporate epistemic uncertainties associated with seismic source characterization, seismicity recurrence parameters,* M_{max}*, and ground motion prediction equations (GMPEs). The framework consists of four hierarchical branching levels representing: (i) three alternative seismic source models (areal, linear fault-based, and gridded point sources), (ii) three alternative β-value branches (β - σβ, β, and β + σβ) accounting for uncertainty in GR recurrence parameters, (iii) two upper bound magnitude branches (*M_{max} *and* M_{max} *+ 0.5) derived using the Kijko[69] statistical estimation approach and (iv) four GMPEs weighted according to their relative statistical performance obtained from LLH analysis. The combination of all epistemic branches results in a total of 72 logic tree branches (3×3×2×4), enabling systematic propagation of uncertainty into the final seismic hazard estimates for the study area.*

PSHA

PSHA provides probabilistic estimates of ground motion intensity in terms of PGA and Peak Spectral Acceleration (PSA) by considering the uncertainties in earthquake occurrence, magnitude, and attenuation. The method assumes that earthquakes occur independently, following a Poisson distribution, and integrates seismic hazard contributions from multiple sources. The fundamental mathematical formulation for computing the exceedance rate of a given ground motion level is expressed as:

$$\nu_z = \sum_{i=1}^{n} \lambda_i \int_{m_o}^{M_u} \int_0^{r_{max}} f_i(m)\, f_i(r)\, P(Z > z|m,r)\ dr dm \quad (7)$$

where ν_z is the average annual rate of excess of a ground movement level z at a site, λ_i is the average frequency of occurrence of an earthquake exceeding m_o at a source i, $f_i(m)$ and $f_i(r)$ are probability distribution functions for magnitude and distance, respectively, and $P(Z > z|m,r)$ is given by a GMPE. The probability that a given ground motion Z (PGA or PSA) will exceed a specified level z at a site within a time period of T years is determined as

$$P[Z_T > z] = 1 - \exp\left(-\nu_z T\right) \quad (8)$$

PSHA for the study region is conducted using the R-CRISIS software, developed by Ordaz and Salgado-Gálvez[82], following the methodology initially proposed by Cornell[25].

Seismic hazard calculations are performed over the study region using a uniform grid spacing of 0.1° × 0.1°, resulting in a total of 15,600 nodes. PGA and PSA at 0.1 s and 1.0 s are computed for 10% and 2% Probability of Exceedance (PoE) in 50 years, corresponding to Return Periods (RP) of 475 and 2475 years, respectively. Earthquake magnitudes are discretized in intervals of 0.1 magnitude units, and source-to-site distances are discretized at 1 km intervals, considering contributions from seismic sources within a maximum distance of 500 km. Hazard curves are obtained by integrating contributions from areal, linear, and point sources across all 72 logic tree branches, thereby incorporating uncertainties in seismicity parameters, maximum magnitude, and ground motion prediction.

Results and Discussion

Seismic hazard is estimated over the study region using a uniform grid spacing of 0.1° × 0.1° in terms of PGA and spectral acceleration (SA) at 0.1 s and 1.0 s for 10% and 2% PoE in 50 years using R-CRISIS[83] software. Bedrock-level PGA varies spatially from ~0.01-0.40 g (10% PoE) to ~0.01-0.70 g (2% PoE in 50 years), with elevated values of 0.25-0.40 g and 0.40-0.70 g, respectively, concentrated along the Andaman-Nicobar arc and northern Sumatra (Fig. 9). These patterns reflect the dominant influence of the Sunda megathrust, forearc segmentation, and intraplate deformation within the Wharton Basin. According to IS 1893 (latest BIS 2025 revision), the Andaman-Nicobar Islands fall within Seismic Zone V (zone factor 0.36 g for 475-year return period). The hazard levels obtained here are broadly comparable to, and in several offshore and southern segments exceed, this prescribed value, while 2475-year PGA values substantially surpass it, underscoring the inability of uniform zone factors to capture the strong spatial variability inherent to this tectonic setting.

The present results are broadly consistent with earlier PSHA investigations but are higher in several areas due to improvements in catalog completeness, source characterization, and uncertainty treatment. Khalqillah et al.[84] reported PGA values up to 2.44 g and short period spectral accelerations exceeding 5.0 g along parts of southern Sumatra; however, these represent the upper bound of reported hazard from event-based rupture simulations and are not directly comparable to the classical Cornell[25] PSHA framework used here. Ornthammarath[85] estimated bedrock PGA of 0.6-1.0 g at a 2475-year RP near the subduction zone but significantly lower hazard (0.05-0.15 g for 475-year RP) along the Thai-Myanmar coast; the present study yields higher and more spatially continuous hazard across the Andaman-Nicobar arc, attributable to refined megathrust geometry and updated seismicity. Susilo et al.[86] reported moderate hazard (PGA ≈ 0.09-0.29 g for a 500-year RP) owing to coarse source zoning and limited offshore constraints. The first dedicated PSHA for the Andaman-Nicobar Islands by Kolathayar and Sitharam[16] reported PGA values of 0.40-0.45 g for 10% PoE and 0.70-0.80 g for 2% PoE in 50 years, with spectral accelerations approaching 1.0 g at 1.0 s. The present results are comparable to, and in several cases exceed, these estimates particularly at longer periods. Petersen et al.[87] predicted ground motions of approximately 0.06-1.0 g (10% PoE) and >1.0 g (2% PoE) across Sumatra but likely underestimated megathrust potential due to limited rupture segmentation. Collectively, these comparisons suggest that earlier studies generally underestimated seismic hazard in parts of the Andaman-Sumatra region, and that the present study provides a more robust and balanced assessment bridging classical and event-based approaches.

The present results are also compared with the GSHAP global hazard map[88] and the GEM Global Seismic Hazard Map version 2023.1[89], computed using OpenQuake for reference rock conditions (Vs30 = 760–800 m/s). GSHAP predicts PGA of 0.25-0.40 g along the Sunda margin for 10% PoE in 50 years, with relatively smooth spatial gradients due to coarse regional source characterization and limited megathrust segmentation. The GEM GSHM-2023 indicates higher values of approximately 0.60 g over the Andaman Islands, 0.50 g over the Nicobar segment, and 0.35-0.55 g over northern Sumatra including Banda Aceh, for the same RP. The present study yields PGA of 0.25-0.40 g across these regions, with elevated values along the subduction interface. The spatial pattern of highest hazard concentrated along the Sunda subduction front and Andaman-Nicobar arc, remaining elevated over northern Sumatra and decreasing eastward toward mainland Thailand and Malaysia, is broadly consistent across all three models. The GEM GSHM-2023 model predicts comparatively higher PGA values over parts of the Andaman Islands. These differences likely arise from variations in megathrust source characterization and the use of globally calibrated GMPEs without region specific statistical weighting. In contrast, the present study employs a higher resolution 0.1° × 0.1° computational grid together with region specific magnitude homogenization and LLH-based GMPE weighting. Epistemic uncertainties are further incorporated through a 72-branch logic tree framework. These improvements provide more internally consistent hazard estimates for the Andaman-Sumatra region. These two models converge more closely over northern Sumatra, providing additional confidence in the adopted framework. While both GSHAP and GEM offer valuable global benchmarks, neither fully captures the extreme ground motions and strong spatial variability associated with large megathrust and intraplate earthquakes.

To assess whether this offset lies within model uncertainty, hazard curves incorporating the logic-tree epistemic range (5th, 50th and 95th percentiles) were compared directly with the GEM GSHM-2023[89] estimates at seven representative sites (Fig. 12). The GEM PGA values (0.45–0.60 g at 10% PoE in 50 years) exceed the 95th percentile of the present logic-tree distribution (0.24–0.36 g) at all sites, indicating that the difference is systematic rather than a consequence of epistemic uncertainty. The discrepancy is largest over the Andaman Islands (GEM ≈ 0.60 g versus a 95th percentile of ≈ 0.24 g) and smallest near the Sumatran megathrust (Meulaboh: GEM ≈ 0.45 g versus ≈ 0.36 g). This offset is attributable to (i) the declustered, Poissonian catalogue adopted here (Gardner and Knopoff[37] removes ~73% of events, lowering activity rates), (ii) region-specific LLH weighting that assigns 0.78 to Lin and Lee[73], which predicts lower motions for this subduction setting than the globally calibrated GMPEs used by GEM, and (iii) differences in megathrust source characterization and spatial resolution. GEM thus provides a conservative global benchmark, whereas the present estimates are more representative of the regional dataset.

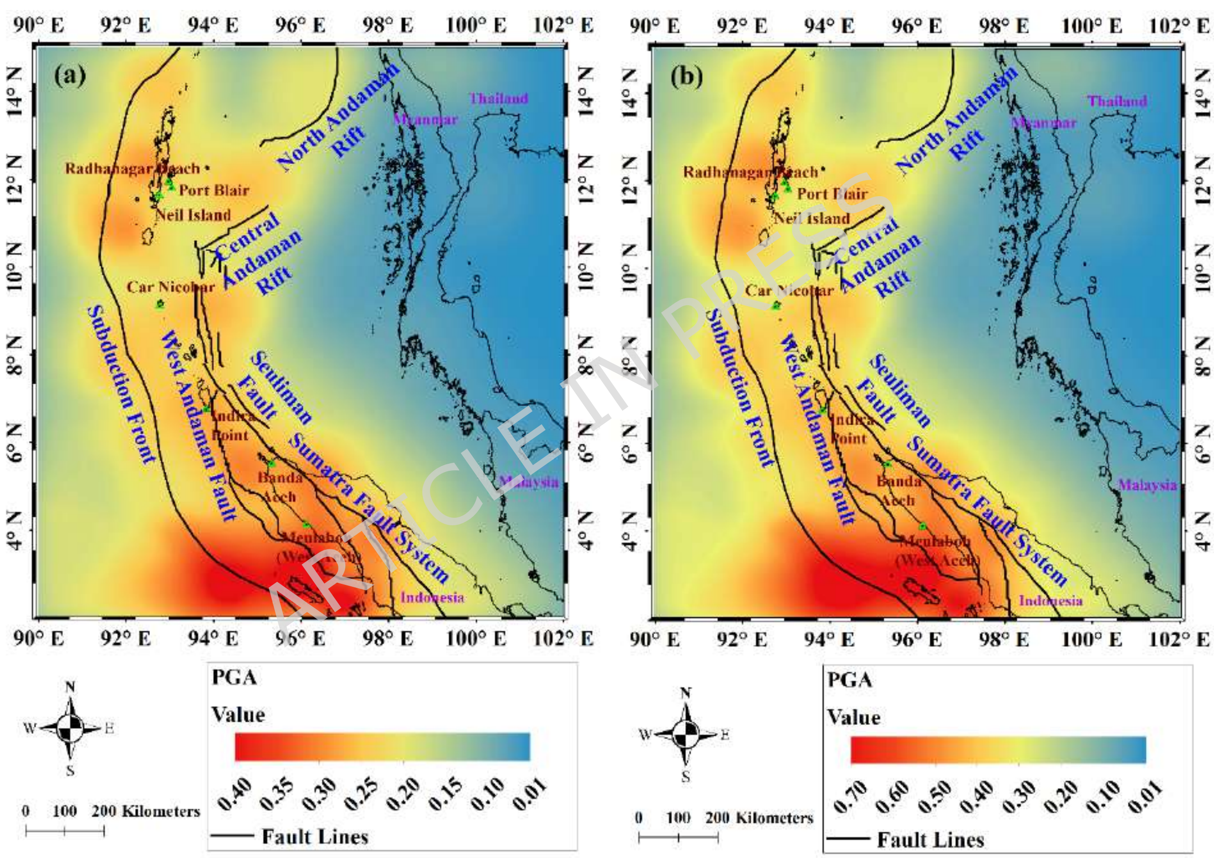

__Fig. 9.__ PGA for the Andaman-Sumatra region. (a) PGA for 10% PoE in 50 years, showing moderate seismic hazard concentrated along the Andaman-Nicobar arc and northern Sumatra, reflecting the influence of the Sunda megathrust and associated active fault systems. (b) PGA for 2% PoE in 50 years, indicating higher ground motion associated with rare large megathrust earthquakes, mainly affecting the Nicobar Islands and offshore Sumatra. The spatial variation in PGA values is represented using a continuous color gradient, where warmer colors (red to orange) indicate regions of higher seismic hazard and cooler colors (green to blue) represent relatively lower hazard levels. Major tectonic structures including the Sunda Subduction Front, West Andaman Fault, Central Andaman Rift, North Andaman Rift, Seuliman Fault, and Sumatra Fault System are superimposed as black solid lines for tectonic reference, while selected key locations are annotated using green triangular symbols for subsequent site-specific hazard interpretation. Map generated by the authors using Esri ArcGIS Desktop 10.8.2 (ArcMap; Esri Inc., Redlands, CA, USA; https://www.esri.com).

Fig. 10 illustrates the spatial distribution of SA at periods of 0.1 s and 1.0 s for 10% and 2% PoE in 50 years. For 10% PoE in 50 years, SA values at 0.1 s range from 0.06 g to 0.77 g, with comparatively higher values (0.56-0.77 g) concentrated along the subduction interface (Fig. 10a). At 1.0 s, SA values range from 0.04 g to 0.70 g, with elevated values (0.51-0.70 g) mainly concentrated along the southern segment of the subduction interface (Fig. 10b). For 2% PoE in 50 years, SA values range from 0.01 g to 1.80 g at 0.1 s and from 0.01 g to 1.40 g at 1.0 s (Fig. 10c and 10d). Overall, higher SA values are observed along the subduction interface, with relatively greater hazard concentrated along the southern segment compared to the northern part of the interface. The elevated SA values along the southern segment of the subduction interface may be attributed to higher seismic activity and the greater potential for large megathrust earthquakes in this region. These results highlight the increased ground motion levels associated with rare, large magnitude megathrust events, particularly affecting offshore Sumatra and the Nicobar Islands. This spatial pattern is consistent with the tectonic setting of the Andaman-Sumatra subduction system, where megathrust earthquakes dominate the regional seismic hazard. Overall, the results indicate that seismic hazard increases toward the southern segment of the Andaman-Sumatra subduction system, particularly near the Sumatra margin.

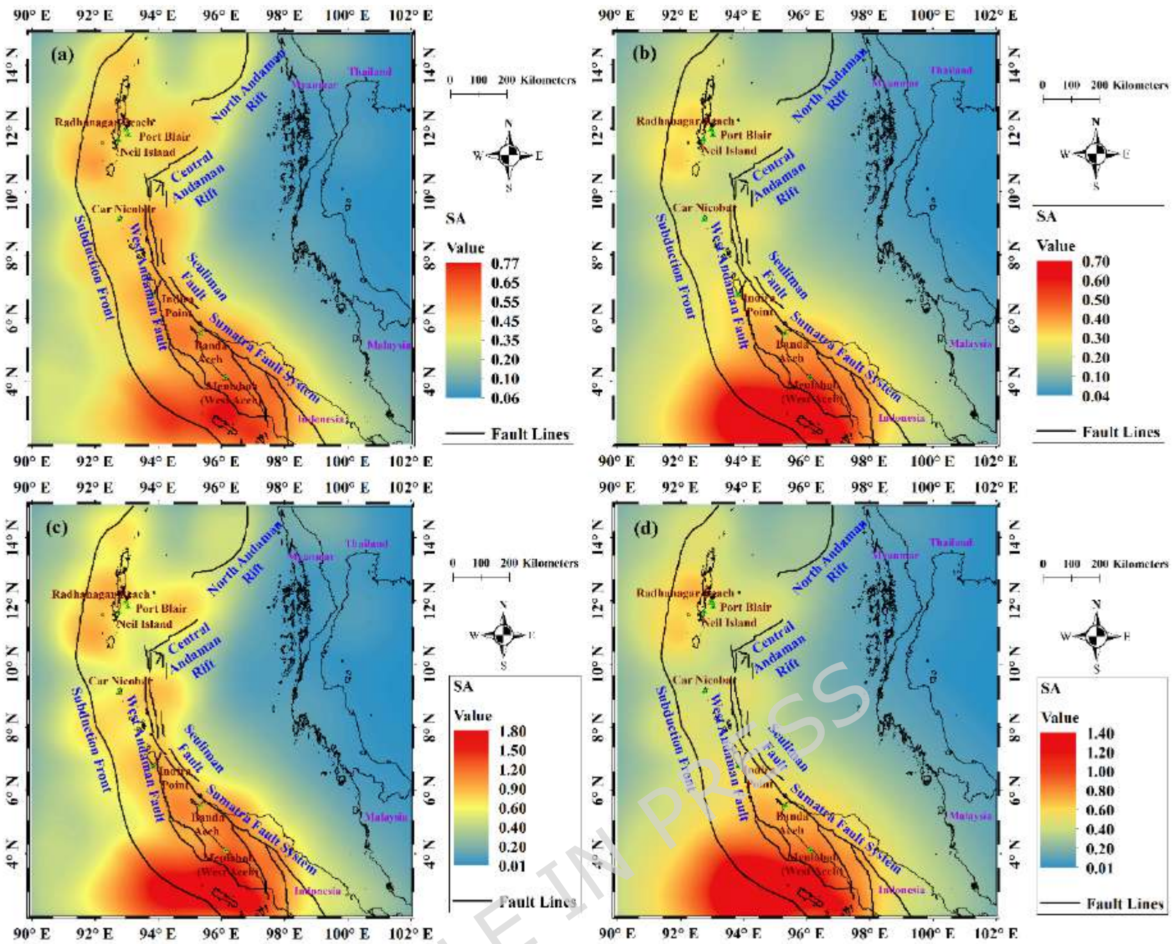

Fig. 10. Spatial distribution of SA values for the Andaman-Sumatra region derived from PSHA considering combined contributions from areal, linear fault-based, and point source seismicity models through the adopted logic tree framework. (a) SA at 0.1 s for 10% PoE in 50 years, representing short period ground motion hazard associated with design level seismic events; (b) SA at 1.0 s for 10% PoE in 50 years, illustrating long period seismic response characteristics for the same hazard level; (c) SA at 0.1 s for 2% PoE in 50 years, corresponding to rare extreme short period ground motions; and (d) SA at 1.0 s for 2% PoE in 50 years, representing long period hazard associated with low probability large magnitude earthquakes. The spatial variation in SA values is represented using a continuous color gradient, where warmer colors (red to orange) indicate regions of elevated seismic hazard and cooler colors (green to blue) indicate comparatively lower hazard levels. Higher SA values are predominantly concentrated along the Sunda Subduction Front, Nicobar segment, northern Sumatra, and associated active tectonic structures due to the influence of megathrust and crustal fault seismicity. Major tectonic features including the Sunda Subduction Front, West Andaman Fault, Central Andaman Rift, North Andaman Rift, Seuliman Fault, and Sumatra Fault System are superimposed as black solid lines for tectonic reference, while selected key locations are indicated using green triangular symbols for site specific hazard interpretation. Map generated by the authors using Esri ArcGIS Desktop 10.8.2 (ArcMap; Esri Inc., Redlands, CA, USA; https://www.esri.com).

Bedrock-level hazard curves and uniform hazard spectra (UHS) for seven representative locations are shown in Figs. 11 and 12. The hazard curves indicate systematic reduction in PoE with increasing PGA and demonstrate significant spatial variability in regional seismic hazard (Fig. 11). Meulaboh and Banda Aceh exhibit the highest hazard levels owing to their close proximity to the Sunda megathrust, whereas comparatively lower hazard levels are observed at Neil Island and Car Nicobar. The UHS results show SA increasing to peak values at short-to-intermediate periods (~0.2-0.3 s) followed by gradual reduction at longer periods. For 10% PoE in 50 years, spectral accelerations range from approximately 0.20-0.78 g (Fig. 13a), while for 2% PoE in 50 years they increase to approximately 0.30-1.45 g (Fig. 13b). The highest spectral accelerations are consistently observed at Meulaboh and Banda Aceh, highlighting the elevated hazard associated with the southern segment of the study area. These results emphasize the importance of site specific design spectra for seismic resistant infrastructure development in the region.

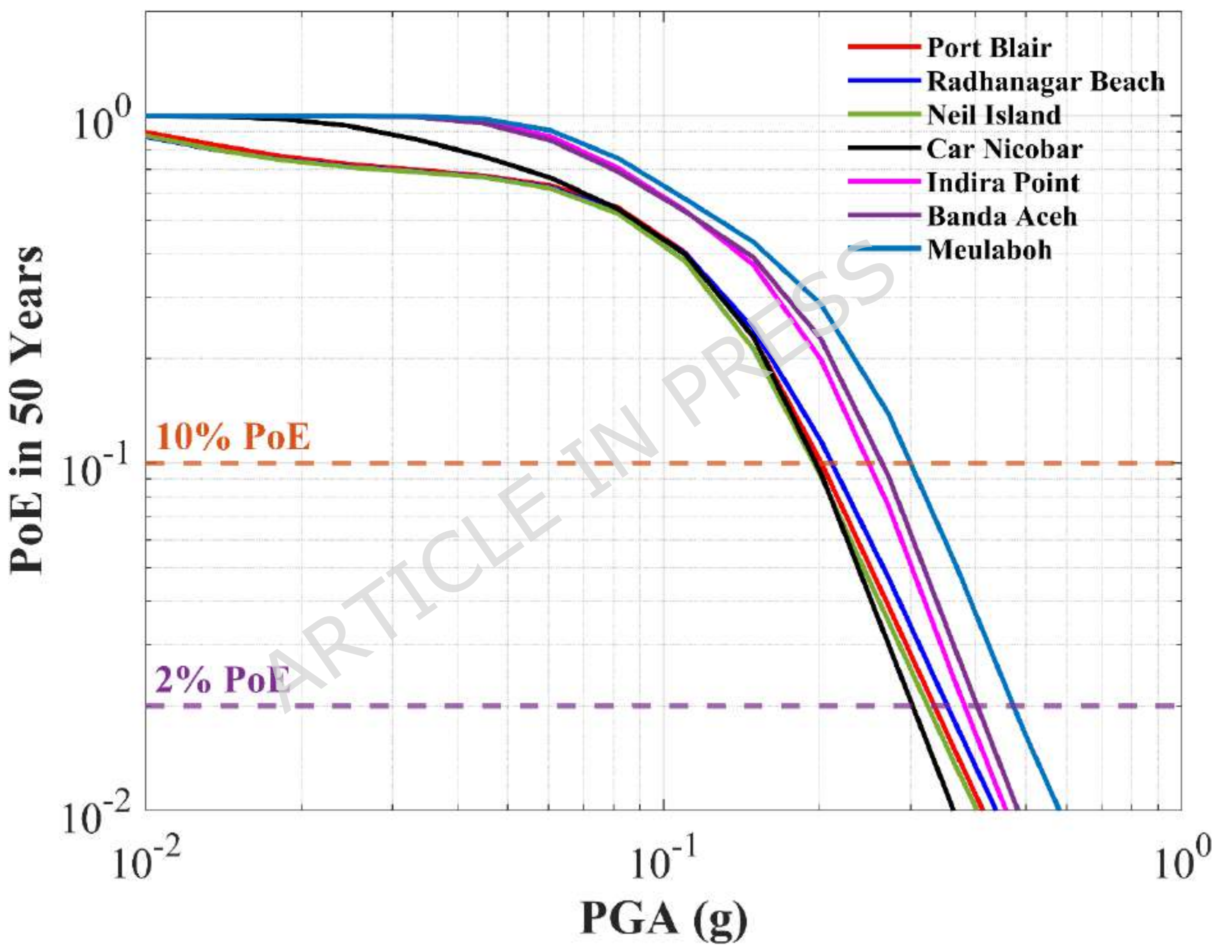

Fig. 11. *Bedrock-level probabilistic seismic hazard curves showing the variation of PGA with PoE in 50 years for the seven selected locations in the Andaman-Sumatra region, namely Port Blair, Radhanagar Beach, Neil Island, Car Nicobar, Indira Point, Banda Aceh, and Meulaboh (West Aceh). The hazard curves were derived from the integrated PSHA considering contributions from areal, linear fault-based, and gridded point source seismicity models through the adopted logic tree framework. Colored solid lines represent the hazard curves corresponding to individual locations, illustrating spatial variability in seismic hazard associated with differing proximity to the Sunda megathrust, Andaman rift system, and associated active tectonic structures. The horizontal dashed lines indicate the standard hazard levels corresponding to 10% and 2% PoE in 50 years, commonly associated with design level and maximum considered earthquake ground motions, respectively. Figure prepared by the authors using MATLAB R2022b (The MathWorks Inc.; https://www.mathworks.com).*

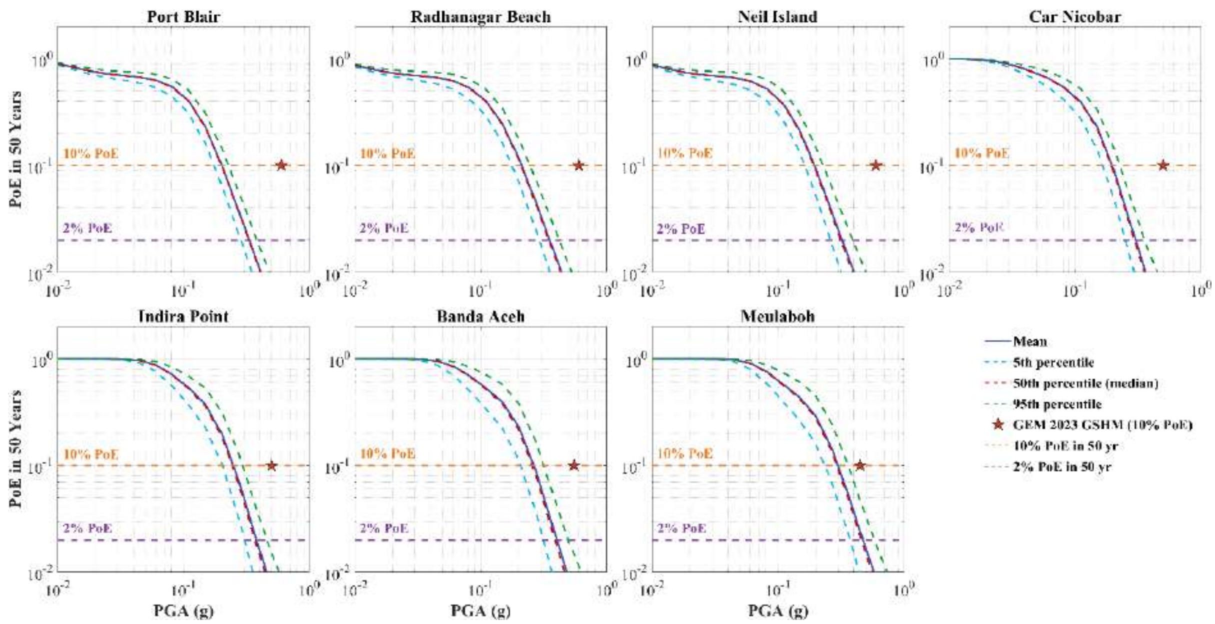

Fig. 12. *Bedrock-level probabilistic seismic hazard curves incorporating logic-tree epistemic uncertainty for the seven selected locations in the Andaman-Sumatra region, namely Port Blair, Radhanagar Beach, Neil Island, Car Nicobar, Indira Point, Banda Aceh, and Meulaboh (West Aceh). For each site the mean hazard curve is shown together with the 5th, 50th (median), and 95th percentile curves derived from the 72-branch logic tree, representing the epistemic dispersion associated with the Gutenberg-Richter and maximum-magnitude parameters. The red star denotes the GEM GSHM-2023 PGA at the 475-year return period (10% PoE in 50 years) extracted at each location for comparison. The horizontal dashed lines indicate the standard hazard levels corresponding to 10% and 2% PoE in 50 years, commonly associated with design level and maximum considered earthquake ground motions, respectively. Figure prepared by the authors using MATLAB R2022b (The MathWorks Inc.; https://www.mathworks.com).*

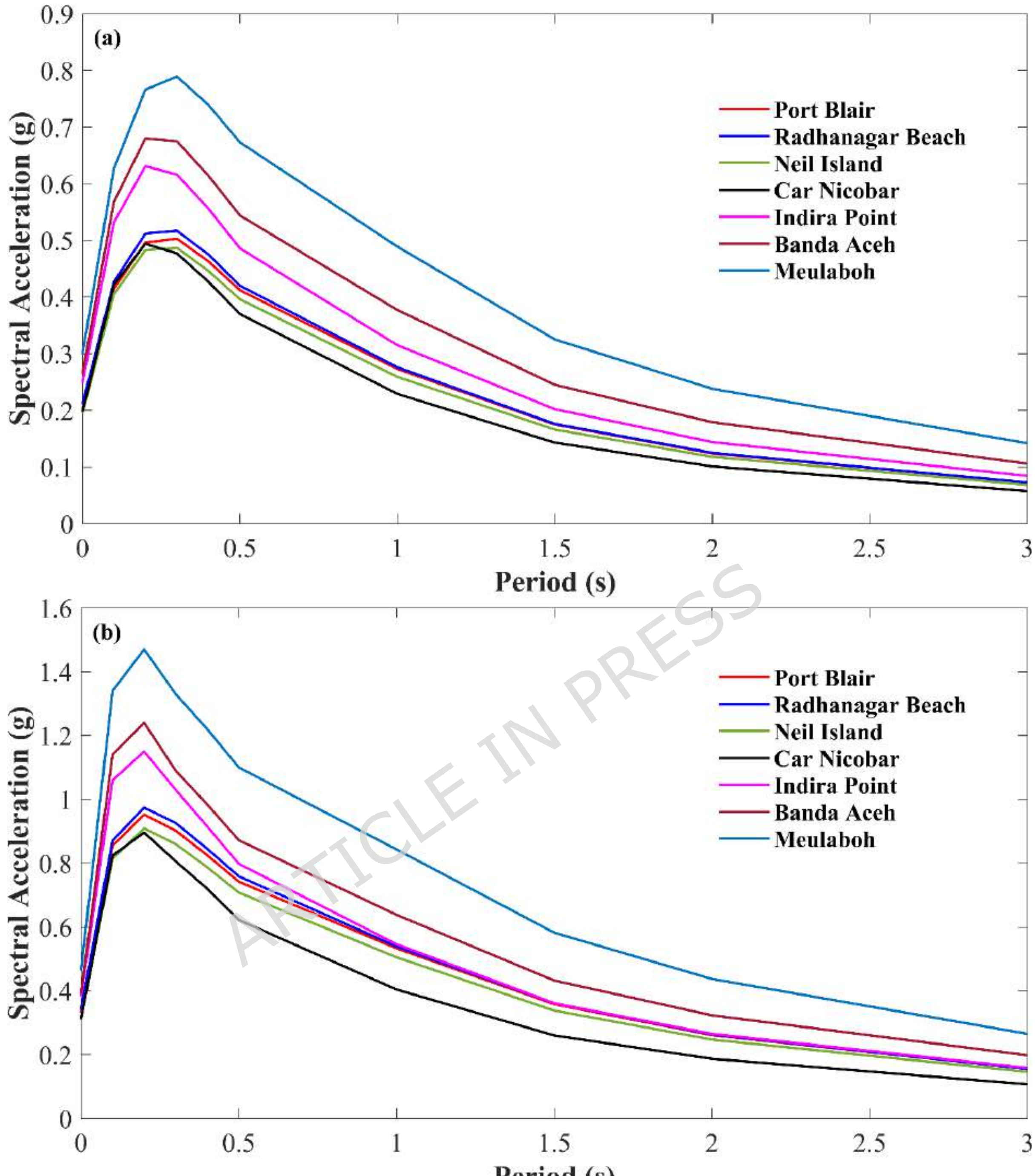

Fig. 13. *Bedrock-level UHS derived from the PSHA for the seven selected locations in the Andaman-Sumatra region, namely Port Blair, Radhanagar Beach, Neil Island, Car Nicobar, Indira Point, Banda Aceh, and Meulaboh (West Aceh). (a) UHS corresponding to 10% PoE in 50 years, representing the design level seismic hazard spectrum, and (b) UHS corresponding to 2% PoE in 50 years, representing the maximum considered earthquake hazard level. The spectra illustrate the variation of SA with structural period and highlight significant spatial differences in seismic hazard due to varying proximity to the Sunda megathrust, Andaman rift system, and associated active tectonic structures. Figure prepared by the authors using MATLAB R2022b (The MathWorks Inc.; https://www.mathworks.com).*

Conclusion

This study provides a refined PSHA of the Andaman-Nicobar and Sumatra regions that captures the combined influence of megathrust, upper-plate, and intraplate seismicity within a unified uncertainty framework. The resulting hazard patterns highlight strong spatial variability, with elevated ground motion levels concentrated along the Andaman-Nicobar arc and Northern Sumatra, reflecting the dominant role of the Sunda megathrust and associated fault systems. These findings reinforce the importance of explicitly accounting for complex source geometries and uncertainty in subduction zone hazard assessments.

Comparison with previous regional and global models indicates that seismic hazard in parts of the Andaman-Sumatra system has likely been underestimated in earlier studies, particularly for long RP relevant to critical infrastructure. The hazard levels obtained here exceed uniform code-based zonation values in several areas, underscoring the limitations of simplified seismic zoning in tectonically complex regions. The results demonstrate the necessity of site- and region-specific PSHA for informed seismic design, risk mitigation, and planning in the Andaman-Nicobar Islands and adjacent offshore domains. The major findings of the present study are as follows:

- Bedrock PGA ranges from ~0.01–0.40 g (475-year RP) and ~0.01–0.70 g (2475-year RP) across the Andaman-Sumatra region. Highest hazard occurs along the Andaman-Nicobar arc and Northern Sumatra, controlled by the Sunda megathrust and active intraplate sources.
- Significant spatial variability of seismic hazard is observed due to megathrust segmentation, forearc tectonics, and distributed deformation. Hazard levels for the 2475-year RP exceed BIS Zone V design acceleration, indicating limitations of zonation based seismic codes.
- SA values reach up to ~0.77 g (0.1 s) and ~0.70 g (1.0 s) for 10% PoE in 50 years, with the highest values concentrated along the subduction interface. For 2% PoE in 50 years, SA increases significantly to ~1.50 g (0.1 s) and ~1.40 g (1.0 s), reflecting the influence of rare large megathrust earthquakes.
- Seismic hazard increases toward the southern segment of the Andaman-Sumatra subduction zone, particularly near offshore Sumatra and the Nicobar region.
- Meulaboh and Banda Aceh exhibit the highest seismic hazard, while Car Nicobar and Neil Island show comparatively lower hazard levels.

- UHS peak at ~0.2-0.3 s, indicating greater vulnerability of short- to intermediate-period structures. Higher hazard levels are primarily controlled by proximity to the Sunda megathrust, which dominates the regional seismic hazard.

Overall, this work contributes a robust, high-resolution hazard model for one of the world's most seismically active subduction systems and provides a methodological framework that can be extended to other complex plate-boundary environments as improved data and modeling approaches become available.

Author Contributions Statement

S S: Conceptualization, Methodology, Data curation, Formal analysis, Investigation, Software, Visualization, Validation, Writing- original draft, Writing- review and editing. **M S:** Supervision, Formal analysis, Writing-original draft and editing. **P N S R:** Supervision, Resources, Writing-review and editing. All authors reviewed and approved the final version of the manuscript.

Data and Resources

The earthquake catalog and processed datasets used in this study are available from the corresponding author upon reasonable request.

Acknowledgement

The first author sincerely acknowledges the Indian Institute of Technology (IIT) Kharagpur for providing the institutional fellowship and computational facilities that were essential for the successful completion of this research. The authors also express their gratitude to Wiemer[40] for the *ZMAP* software used in seismicity analysis and to the developers of the *R-CRISIS* software package[83], which significantly supported this study. All figures in this study were prepared by the authors using Esri ArcGIS Desktop 10.8.2 (ArcMap; https://www.esri.com) and MATLAB R2022b (The MathWorks Inc.; https://www.mathworks.com). The authors extend their sincere gratitude to the handling editors, Dr. Niptika Jana and Dr. Claire Potter, as well as the anonymous reviewers for their constructive comments and valuable suggestions, which substantially improved the quality and clarity of the manuscript. The authors extend their heartfelt thanks to Dr. Haritha Chandriyan for her valuable insights and constructive suggestions throughout the course of this research. Special appreciation is also conveyed to Shuvankar Samantara, Priyank Pathak, and Anupama Sharma for fostering a supportive, peaceful, and motivating research environment.

Funding Declaration

Not applicable.

Additional Information

Competing interests

The authors declare no competing interests.

References

1. Lay, T., Yue, H., Brodsky, E. E. & An, C. The 1 April 2014 Iquique, Chile, mw 8.1 earthquake rupture sequence. *Geophys. Res. Lett.* **41**, 3818–3825 (2014).

2. Schellart et al., 2007. Evolution and diversity of subduction zones controlled by slab width. *Nature* **446**, 308–311 (2007).

3. Chlieh, M., Avouac, J. P., Sieh, K., Natawidjaja, D. H. & Galetzka, J. Heterogeneous coupling of the Sumatran megathrust constrained by geodetic and paleogeodetic measurements. *{Journal Geophys. Res. Solid Earth* **113**, 1–31 (2008).

4. Gahalaut, V. K., Nagarajan, B., Catherine, J. K. & Kumar, S. Constraints on 2004 Sumatra – Andaman earthquake rupture from GPS measurements in Andaman – Nicobar Islands. *Earth Planet. Sci. Lett.* **242**, 365–374 (2006).

5. Prawirodirdjo, L. & Bock, Y. Instantaneous global plate motion model from 12 years of continuous GPS

observations. *J. Geophys. Res. Solid Earth* **109**, 1–15 (2004).

6. Ammon, C. J. *et al.* Rupture Process of the 2004 Sumatra-Andaman Earthquake. *Science (80-.).* 1133–1139 (2005).

7. Vigny, C. *et al.* Insight into the 2004 Sumatra – Andaman earthquake from GPS measurements in southeast Asia. *Nature* **436**, 201–206 (2005).

8. Fujii, Y. & Satake, K. Tsunami Source of the 2004 Sumatra – Andaman Earthquake Inferred from Tide Gauge and Satellite Data. *Bull. Seismol. Soc. Am.* **97**, 192–207 (2007).

9. Walker, K. T., Ishii, M. & Shearer, P. M. Rupture details of the 28 March 2005 Sumatra M w 8 . 6 earthquake imaged with teleseismic P waves. *Geophys. Res. Lett.* **32**, 1–4 (2005).

10. Ishii, M., Shearer, P. M., Houston, H. & Vidale, J. E. Teleseismic P wave imaging of the 26 December 2004 Sumatra-Andaman and 28 March 2005 Sumatra earthquake ruptures using the Hi-net array. *J. Geophys. Res.* **112**, 1–16 (2007).

11. Pichon, A. Le *et al.* Infrasound associated with 2004 – 2005 large Sumatra earthquakes and tsunami. *Geophys. Res. Lett.* **32**, 1–5 (2005).

12. Satriano, C., Kiraly, E., Bernard, P. & Vilotte, J. The 2012 Mw 8 . 6 Sumatra earthquake : Evidence of westward sequential seismic ruptures associated to the reactivation of a N-S ocean fabric. *Geophys. Res. Lett.* **39**, 1–6 (2012).

13. Duputel, Z. *et al.* The 2012 Sumatra great earthquake sequence. *Earth Planet. Sci. Lett.* (2012).

14. Delescluse, M. *et al.* April 2012 intra-oceanic seismicity off Sumatra boosted by the Banda-Aceh megathrust. *Nature* (2012) doi:10.1038/nature11520.

15. Kataria, N. P., Shrikhande, M. & Das, J. D. Deterministic seismic hazard analysis of andaman and nicobar islands. *J. Earthq. Tsunami* **7**, (2013).

16. Kolathayar, S. & Sitharam, T. G. Comprehensive Probabilistic Seismic Hazard Analysis of the Andaman – Nicobar Regions. **102**, 2063–2076 (2012).

17. Sitharam, T. G. & Kolathayar, S. Seismic hazard analysis of India using areal sources. *Journal of Asian Earth Sciences* vol. 62 647–653 (2013).

18. Mishra, M., Yadav, A. R. B. S. & Sandhu, M. Probabilistic assessment of earthquake hazard in the Andaman – Nicobar – Sumatra region. *Nat. Hazards* **105**, 313–338 (2021).

19. Stein, S. & Okal, Æ. E. A. The 2004 Sumatra earthquake and Indian Ocean tsunami : What happened and why ? *Vis. Geosci.* **10**, 21–26 (2005).

20. Abercrombie, R. E. & Antolik, M. The June 2000 M w 7 . 9 earthquakes south of Sumatra : Deformation in the India – Australia Plate. *J. Geophys. Res. Solid Earth* **108**, ESE--6 (2003).

21. Robinson, D. P., Henry, C., Das, S. & Woodhouse, J. H. Simultaneous Rupture Along Two Conjugate Planes of the Wharton Basin Earthquake. *Science (80-.).* **292**, 1145–1148 (2001).

22. Zahoor, F., Ansari, A., Rao, K. S. & Satyam, N. Seismic Hazard Assessment of Kashmir Region Using Logic Tree Approach : Focus on Sensitivity of PSHA Results Towards Declustering Procedures and GMPEs. *Pure Appl. Geophys.* (2023) doi:10.1007/s00024-023-03239-5.

23. Borah, N. & Kumar, A. Probabilistic seismic hazard analysis of the North-East India towards identification of contributing seismic sources. *Geomatics, Nat. Hazards Risk* **14**, 1–38 (2023).

24. Sambath, M., Chandrasekaran, S. S., Maithani, S. & Ganapathy, G. P. Probabilistic seismic hazard analysis of the Coimbatore region, Tamil Nadu using a logic-tree approach. *J. Earth Syst. Sci.* **133**, (2024).

25. Cornell, B. Y. C. A. Engineering seismic risk analysis. *Bull. Seismol. Soc. Am.* **58**, 1583–1606 (1968).

26. Kramer, S. L. *Geotechnical Earthquake Engineering*. (Prentice Hall, 1996).

27. McGuire, R. K. Deterministic vs . probabilistic earthquake hazards and risks. *Soil Dyn. Earthq. Eng.* **21**, 377–384 (2001).

28. McCaffrey, R. The Tectonic Framework of the Sumatran Subduction Zone. *Annu. Rev. Earth Planet. Sci.* **37**, 345--366 (2009).

29. Demets, C., Gordon, R. G. & Argus, D. F. Geologically current plate motions. *Geophys. J. Int.* **81**, 1–80 (2010).

30. Tan, O. A homogeneous earthquake catalogue for Turkey. *Nat. Hazards Earth Syst. Sci.* **21**, 2059–2073 (2021).

31. Shahabuddin, M. & Mohanty, W. K. An Updated and Unified Complete Earthquake Catalog of the Shillong Plateau and Adjoining Region. *Seismol. Res. Lett.* (2025) doi:10.1785/0220240217.Supplemental.

32. Pacor, F. *et al.* Overview of the Italian strong motion database. *Bull Earthq. Eng* 1723–1739 (2011) doi:10.1007/s10518-011-9327-6.

33. Scordilis, E. M. Empirical global relations converting MS and mb to moment magnitude. *J. Seismol.* **10**, 225–236 (2006).

34. Castellaro, S., Mulargia, F. & Kagan, Y. Y. Regression problems for magnitudes. *Geophys. J. Int.* **165**, 913–930 (2006).

35. Weatherill, G. A., Pagani, M. & Garcia, J. Exploring earthquake databases for the creation of magnitude-homogeneous catalogues: Tools for application on a regional and global scale. *Geophys. J. Int.* **206**, 1652–1676 (2016).

36. Tsampas, A. D., Scordilis, E. M., Papazachos, B. C. & Karakaisis, G. F. Global-Magnitude Scaling Relations for Intermediate-Depth and Deep-Focus Earthquakes. *Bull. Seismol. Soc. Am.* **106**, 418–434 (2016).

37. Gardner, J. K. & Knopoff, L. Is sequence of earthquakes in southern california, with aftershocks removed, poissonian? *Bull. Seismol. Soc. Am.* **64**, 1363–1367 (1974).

38. Reasenberg, P. Second-Order Moment of Central California Seismicity, 1969-1982. *J. Geophys. Res.* **90**, 5479–5495 (1985).

39. Uhrhammer, R. A. Characteristics of northern and central California seismicity. *Earthq. Notes* **57**, 21–37 (1986).

40. Wiemer, S. A software package to analyze seismicity: ZMAP. *Seismol. Res. Lett.* **72**, 373–382 (2001).

41. Marzocchi, W. & Taroni, M. Some Thoughts on Declustering in Probabilistic Seismic-Hazard Analysis. **104**, 1838–1845 (2014).

42. Taroni, M. & Akinci, A. Good practices in PSHA : declustering , b-value estimation , foreshocks and aftershocks inclusion ; a case study in Italy Matteo Taroni and Aybige Akinci. 1174–1187 (2021) doi:10.1093/gji/ggaa462.

43. Field, E. H., Milner, K. R. & Luco, N. The Seismic Hazard Implications of Declustering and Poisson Assumptions Inferred from a Fully Time-Dependent Model. 527–537 (2022) doi:10.1785/0120210027.

44. Taroni, M. Reintroducing Aftershocks in PSHA. 2025–2027 (2024) doi:10.1785/0220240391.

45. Das, R. *et al.* Updated probabilistic seismic hazard assessment using M wg (Das magnitude scale) to address moment magnitude (M) scale inaccuracies below 7 . 5 : a case study from Northeast India. 1–26 (2025).

46. Bi, J., Song, C. & Cao, F. Declustering characteristics of the North China Plain seismic belt and its effect on probabilistic seismic hazard analysis. *Sci. Rep.* **14**, 22170 (2024).

47. Montiel-lópez, D. *et al.* Computing the time-dependent activity rate using non-declustered and

declustered catalogues – a first step towards time-dependent seismic hazard calculations for operational earthquake forecasting. 515–539 (2025).

48. Gerstenberger, M. C. *et al.* Probabilistic Seismic Hazard Analysis at Regional and National Scales : State of the Art and Future Challenges. 1–49 (2020) doi:10.1029/2019RG000653.

49. Stepp, J. C. Analysis of completeness of the earthquake sample in the Puget Sound area and its effect on statistical estimates of earthquake hazard. *Proc. Intern. Conf. Microzonat. Safer Const.* **2**, 897–909 (1972).

50. Cattin, R. *et al.* Stress change and effective friction coefficient along the Sumatra-Andaman-Sagaing fault system after the 26 December 2004 (Mw = 9.2) and the 28 March 2005 (Mw = 8.7) earthquakes. *Geochemistry Geophys. Geosystems* **10**, 3 (2009).

51. Frankel, A. Mapping seismic hazard in the central and eastern United States. *Seismol. Res. Lett.* **66**, 8–21 (1995).

52. Woo, G. Kernel estimation methods for seismic hazard area source modeling. *Bull. Seismol. Soc. Am.* **86**, 353–362 (1996).

53. Wahlström, R. & Grünthal, G. Probabilistic Seismic Hazard Assessment (Horizontal PGA) for Fennoscandia Using the Logic Tree Approach for Regionalization and Nonregionalization Models. *Soil Dyn. Earthq. Eng.* 45--58 (2000).

54. Lapajne, Janez and Motnikar, Barbara Sket and Zupancic, P. Probabilistic Seismic Hazard Assessment Methodology for Distributed Seismicity. *Bull. Seismol. Soc. Am.* **93**, 2502–2515 (2003).

55. Jaiswal, K. & Sinha, R. Probabilistic Seismic-Hazard Estimation for Peninsular India. *Bull. Seismol. Soc. Am.* **97**, 318–330 (2007).

56. Vilanova, S. P. & Fonseca, J. F. B. D. Probabilistic Seismic-Hazard Assessment for Portugal. *Bull. Seismol. Soc. Am.* **97**, 1702–1717 (2007).

57. Kalkan, E., Gülkan, P., Yilmaz, N. & Çelebi, M. Reassessment of Probabilistic Seismic Hazard in the Marmara Region. *Bull. Seismol. Soc. Am.* **99**, 2127–2146 (2009).

58. Menon, A., Ornthammarath, T., Corigliano, M. & Lai, C. G. Probabilistic seismic hazard macrozonation of Tamil Nadu in Southern India. *Bull. Seismol. Soc. Am.* **100**, 1320–1341 (2010).

59. Gutenberg, B. & Richter, C. F. Frequency of earthquakes in california. *Bull. Seismol. Soc. Am.* 185–188 (1944).

60. Aki, K. Maximum likelihood estimate of b in the formula log N= a-bM and its confidence limits. *Bull. Earthq. Res. Inst., Tokyo Univ* **43**, 237–239 (1965).

61. Utsu, T. Representation and Analysis of the Earthquake Size Distribution: A Historical Review and Some New Approaches. *Pure Appl. Geophys.* **155**, 509–535 (1999).

62. Rydelek, P. A. & Sacks, I. S. Testing the completeness fo earthquake catalogue and the hypothesis of self-similaity. *Nature* **337**, 251–253 (1989).

63. Wiemer, S. & Wyss, M. Minimum Magnitude of Completeness in Earthquake Catalogs: Examples from Alaska, the Western United States, and Japan. *Bull. Seismol. Soc. Am.* **90**, 859–869 (2000).

64. Reiter, L. *Earthquake Hazard Analysis Issues and Insights*. (Columbia University Press, 1990).

65. Nuannin, P., Kulhánek, O. & Persson, L. Journal of Asian Earth Sciences Variations of b -values preceding large earthquakes in the Andaman – Sumatra subduction zone. **61**, 237–242 (2012).

66. Yáñez, C. M., Bustamante, L., Benavente, R., Sippl, C. & Moreno, M. OPEN B - value variations in the Central Chile seismic gap assessed by a Bayesian transdimensional approach. *Sci. Rep.* 1–12 (2022) doi:10.1038/s41598-022-25338-4.

67. Chiba, K. Stress state along the western Nankai Trough subduction zone inferred from b - values , long - term slow - slip events , and low - frequency earthquakes. *Earth, Planets Sp.* (2020)

doi:10.1186/s40623-020-1130-7.

68. Kijko, A. & Sellevoll, M. A. Estimation of earthquake hazard parameters from incomplete data files. Part I. Utilization of extreme and complete catalogs with different threshold magnitudes. *Bull. - Seismol. Soc. Am.* **79**, 645–654 (1989).

69. Kijko, A. Estimation of the maximum earthquake magnitude, mmax. *Pure Appl. Geophys.* **161**, 1655–1681 (2004).

70. Bommer, J. J. *et al.* On the selection of ground-motion prediction equations for seismic hazard analysis. *Seismol. Res. Lett.* **81**, 783–793 (2010).

71. Delavaud, E. *et al.* Toward a ground-motion logic tree for probabilistic seismic hazard assessment in Europe. *J. Seismol.* **16**, 451–473 (2012).

72. Scherbaum, F., Delavaud, E. & Riggelsen, C. Model selection in seismic hazard analysis: An information-theoretic perspective. *Bull. Seismol. Soc. Am.* **99**, 3234–3247 (2009).

73. Lin, P. S. & Lee, C. T. Ground-motion attenuation relationships for subduction-zone earthquakes in Northeastern Taiwan. *Bull. Seismol. Soc. Am.* **98**, 220–240 (2008).

74. Zhao, J. X. *et al.* Attenuation Relations of Strong Ground Motion in Japan Using Site Classification Based on Predominant Period. *Bull. Seismol. Soc. Am.* **96**, 898–913 (2006).

75. Akkar, Sinan and Bommer, J. J. Empirical equations for the prediction of PGA, PGV, and spectral accelerations in Europe, the Mediterranean region, and the Middle East. *Seismol. Res. Lett.* **81**, 195–206 (2010).

76. Youngs, R. R., Chiou, S. J., Silva, W. J. & Humphrey, J. R. Strong ground motion attenuation relationships for subduction zone earthquakes. *Seismol. Res. Lett.* **68**, 58–73 (1997).

77. Kulkarni, R. B., Youngs, R. R. & Coppersmith, K. J. Assessment of Confidence Intervals for Results

of Seismic Hazard Analysis. in *8th World Conference on Earthquake Engineering* 263–270 (1984).

78. Coppersmith, Youngs, K. J. and & R, R. Probabilistic seismic-hazard analysis using expert opinion; an example from the Pacific Northwest. (1990).

79. Bommer, J. J., Eeri, M. & Scherbaum, F. The Use and Misuse of Logic Trees in Probabilistic Seismic Hazard Analysis. **24**, 997–1009 (2008).

80. Petersen, M. D. *et al. The 2023 US 50-State National Seismic Hazard Model : Overview and implications*. (2024). doi:10.1177/87552930231215428.

81. Rezaeian, S. *et al.* The 2023 US National Seismic Hazard Model : Subduction ground-motion models. (2024) doi:10.1177/87552930241243069.

82. Ordaz, M. & Salgado-Galvez, M. A. *R-CRISIS v20 Validation and Verification document. ERN Technical Report*. (2020).

83. Ordaz, M., Salgado-Gálvez, M. A. & Giraldo, S. R-CRISIS: 35 years of continuous developments and improvements for probabilistic seismic hazard analysis. *Bull. Earthq. Eng.* 2797–2816 (2021) doi:10.1007/s10518-021-01098-w.

84. Khalqillah, A., Muksin, U., Simanjutak, A. V. H., Jihad, A. & Banyunegoro, H. Engineering , Environment , and Technology Seismic Hazard Estimation for Sumatra and Kalimantan Region Using Event-Based Probabilistic Seismic Hazard Analysis (EB-PSHA). *J. Geosci. Eng. Environ. Technol. Environ. Technol.* **10**, 329–337 (2025).

85. Ornthammarath, T. Probabilistic seismic hazard assessment for offshore structures in Andaman Sea. *CRC Press* 2805–2810 (2018).

86. Susilo, A., Adnan, Z. & Member, S. Probabilistic Seismic Hazard Analysis of East Java Region , Indonesia. *Int. J. Comput. Electr. Eng.* **5**, 341–344 (2013).

87. Petersen, M. D. *et al.* Probabilistic seismic hazard analysis for Sumatra , Indonesia and across the Southern Malaysian Peninsula. *Tectonics* **390**, 141–158 (2004).

88. Giardini, D., Grunthal, G., Shedlock, K. M. & Zhang, P. The GSHAP Global Seismic Hazard Map. *Annali di Geofisica* vol. 42 1225–1228 (1999).

89. Johnson, K. *et al.* Global Earthquake Model (GEM) Seismic Hazard Map (version 2023.1 – June 2023). (2023) doi:10.5281/zenodo.8409647.

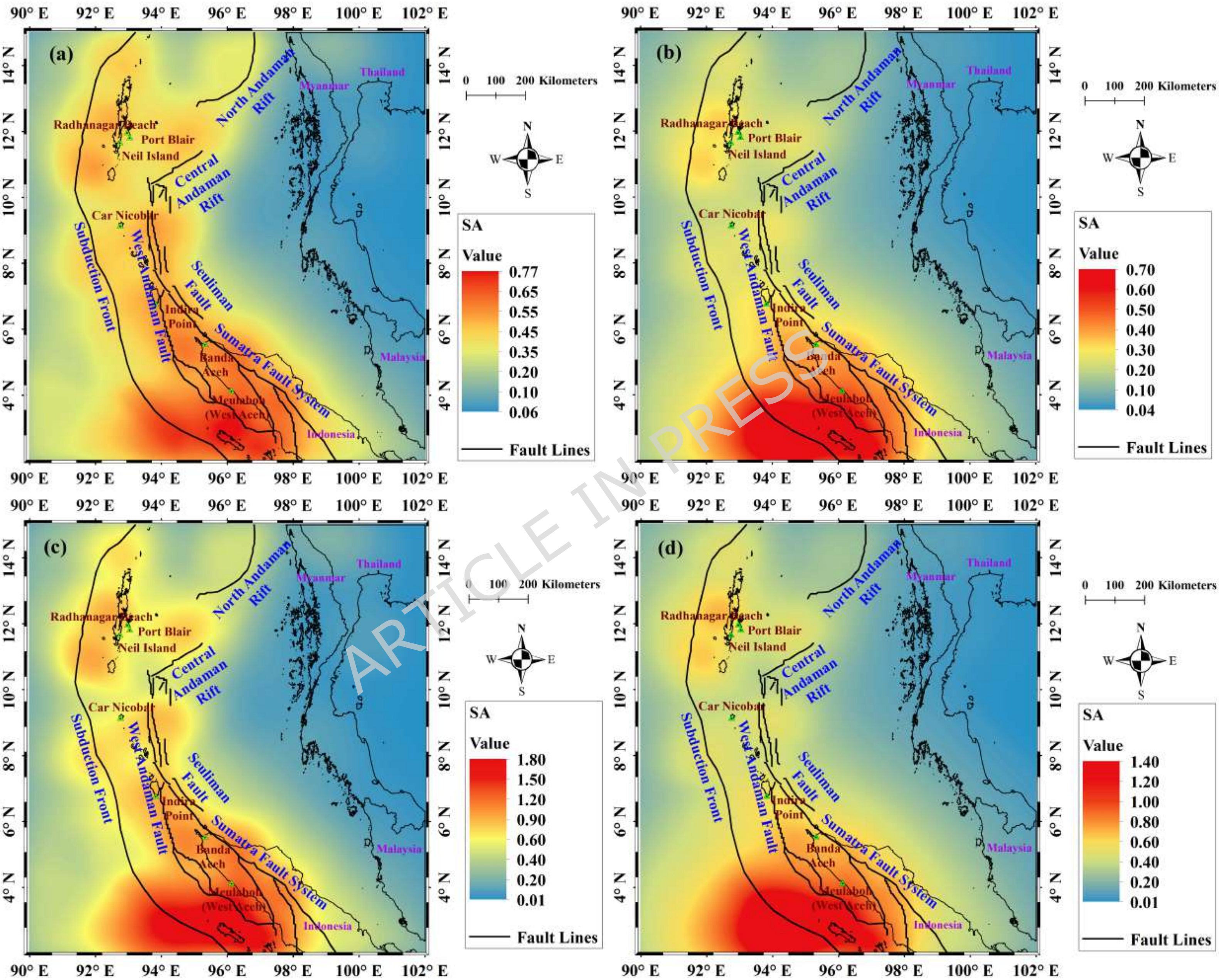
(a)
(b)
(c)
(d)
90° E
92° E
94° E
96° E
98° E
100° E
102° E
14° N
12° N
10° N
8° N
6° N
4° N
Thailand
Myanmar
Malaysia
Indonesia
North Andaman Rift
Central Andaman Rift
Radhanagar Beach
Port Blair
Neil Island
Car Nicobar
Subduction Front
West Andaman Fault
Seuliman Fault
Indira Point
Sumatra Fault System
Banda Aceh
Meulaboh (West Aceh)
0 100 200 Kilometers
N
W
E
S
SA
Value
0.77
0.65
0.55
0.45
0.35
0.20
0.10
0.06
0.70
0.60
0.50
0.40
0.30
0.20
0.10
0.04
1.80
1.50
1.20
0.90
0.60
0.40
0.20
0.01
1.40
1.20
1.00
0.80
0.60
0.40
0.20
0.01
Fault Lines

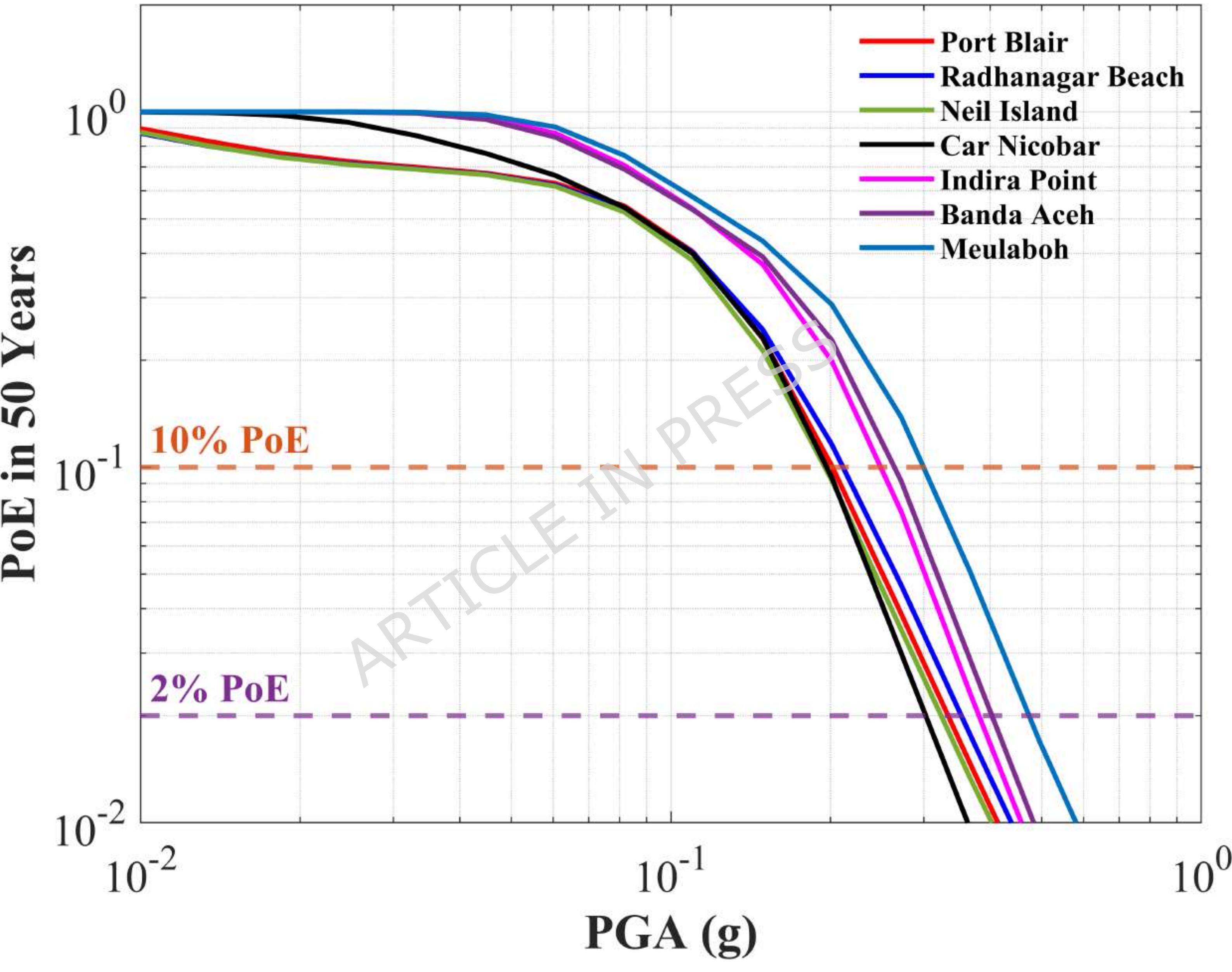
Port Blair
Radhanagar Beach
Neil Island
Car Nicobar
Indira Point
Banda Aceh
Meulaboh
10% PoE
2% PoE
PoE in 50 Years
PGA (g)
10^0
10^{-1}
10^{-2}
10^{-2}
10^{-1}
10^0

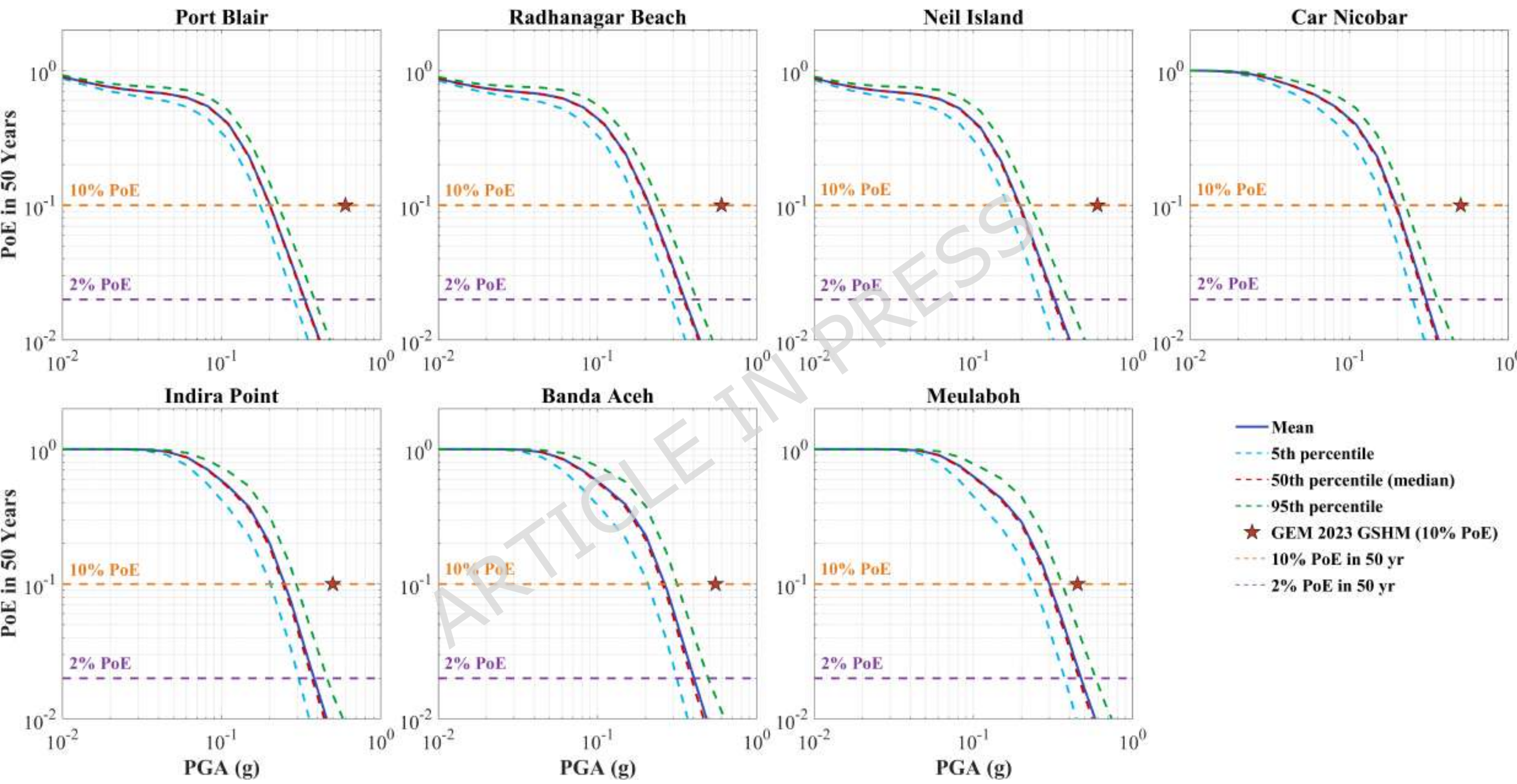
Port Blair
Radhanagar Beach
Neil Island
Car Nicobar
Indira Point
Banda Aceh
Meulaboh
PoE in 50 Years
PGA (g)
10% PoE
2% PoE
Mean
5th percentile
50th percentile (median)
95th percentile
GEM 2023 GSHM (10% PoE)
10% PoE in 50 yr
2% PoE in 50 yr

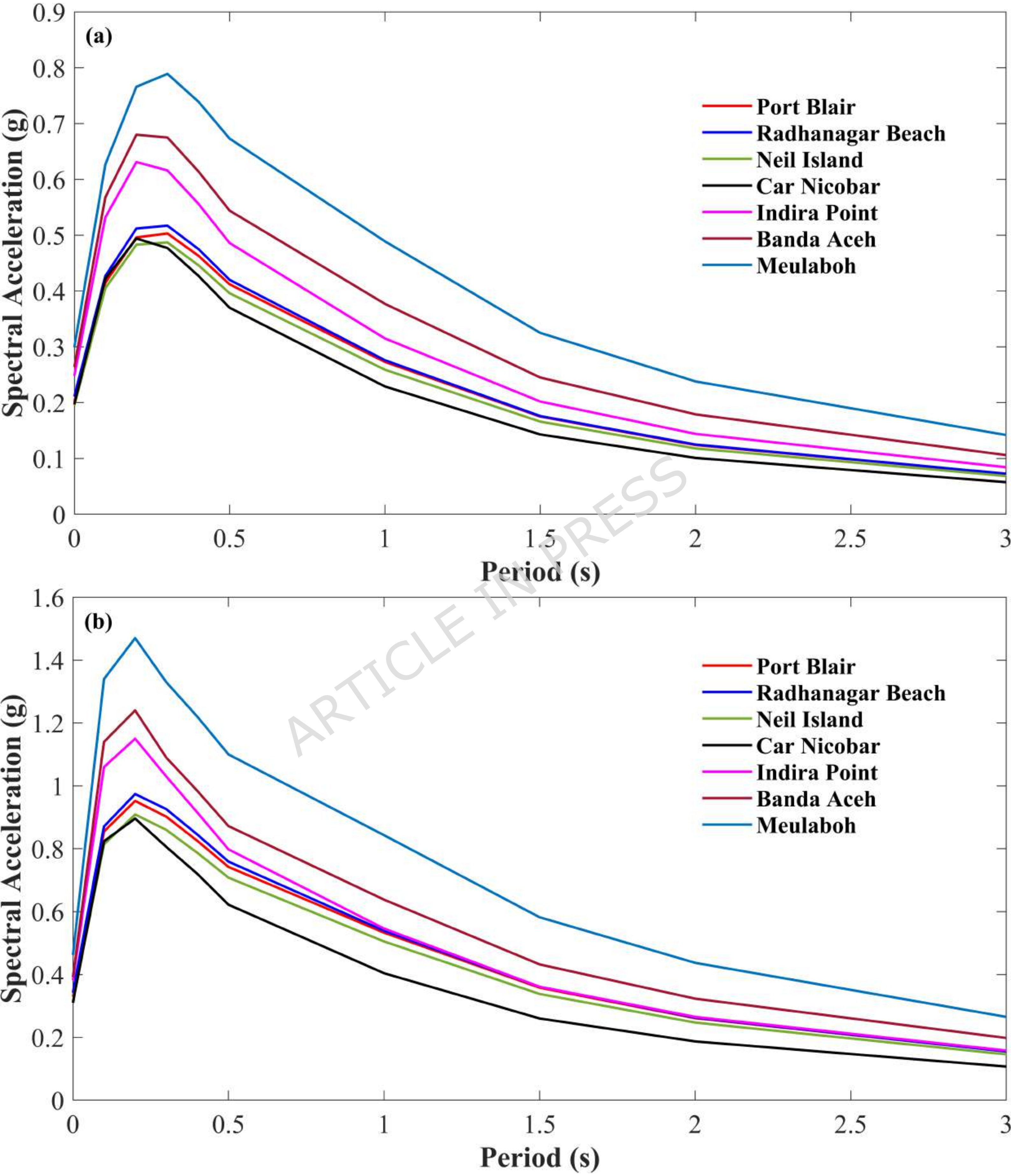

(a)
Spectral Acceleration (g)
0.9
0.8
0.7
0.6
0.5
0.4
0.3
0.2
0.1
0
0.5
1
1.5
2
2.5
3
Period (s)
Port Blair
Radhanagar Beach
Neil Island
Car Nicobar
Indira Point
Banda Aceh
Meulaboh
(b)
Spectral Acceleration (g)
1.6
1.4
1.2
1
0.8
0.6
0.4
0.2
0
0.5
1
1.5
2
2.5
3
Period (s)
Port Blair
Radhanagar Beach
Neil Island
Car Nicobar
Indira Point
Banda Aceh
Meulaboh

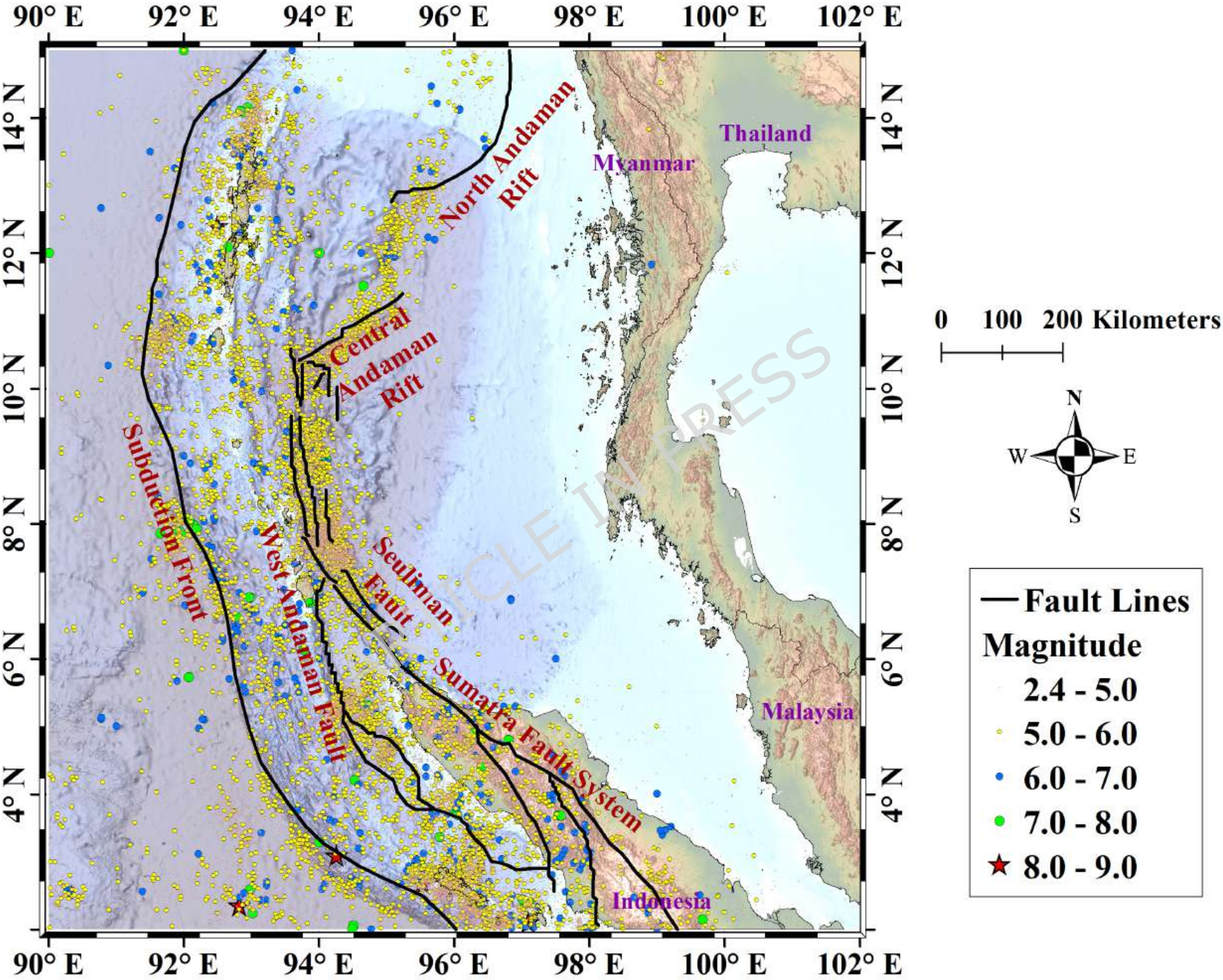
90° E
92° E
94° E
96° E
98° E
100° E
102° E
14° N
12° N
10° N
8° N
6° N
4° N
Thailand
Myanmar
North Andaman Rift
Central Andaman Rift
Subduction Front
West Andaman Fault
Seuliman Fault
Sumatra Fault System
Malaysia
Indonesia
0 100 200 Kilometers
N
W
E
S
Fault Lines
Magnitude
2.4 - 5.0
5.0 - 6.0
6.0 - 7.0
7.0 - 8.0
8.0 - 9.0

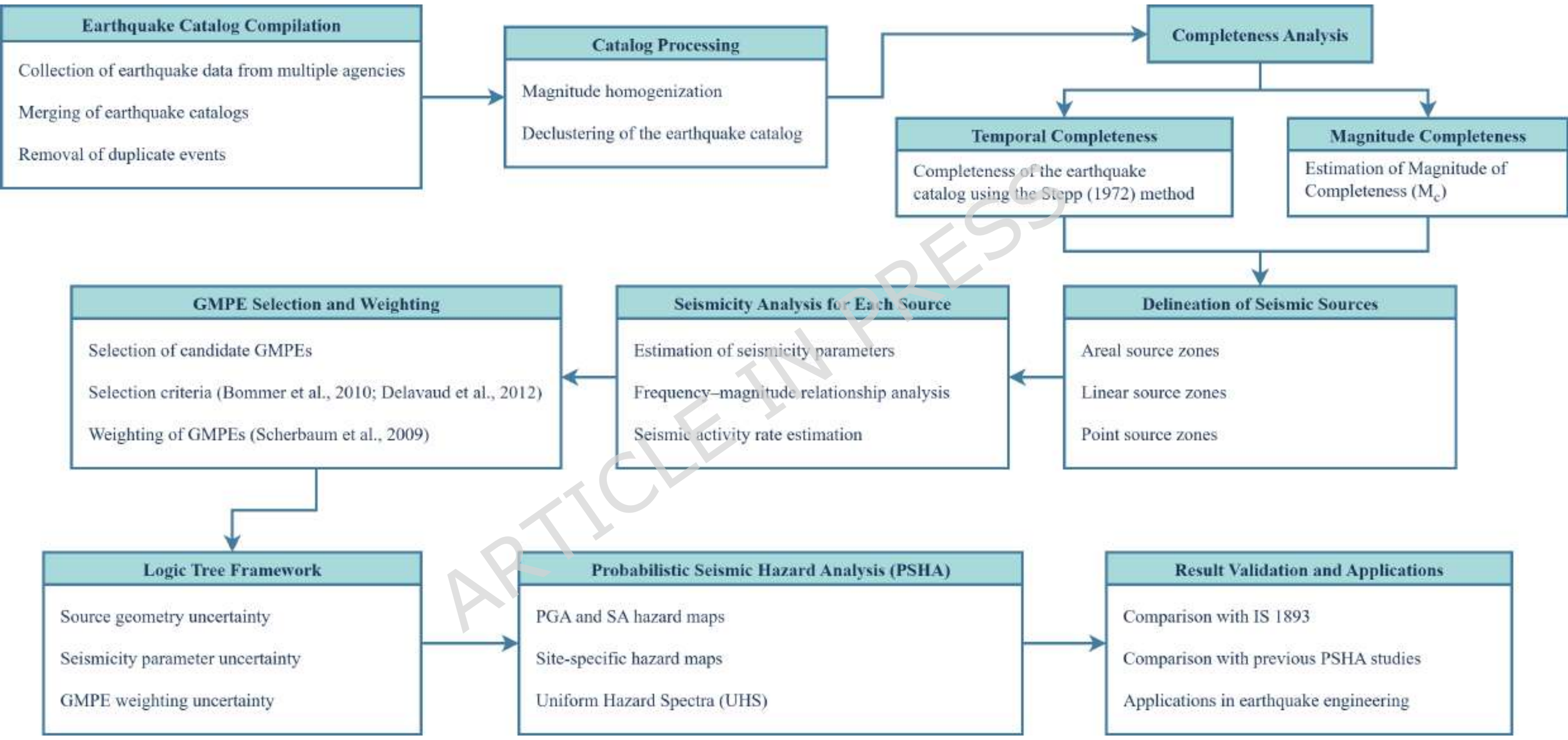
Earthquake Catalog Compilation
Collection of earthquake data from multiple agencies
Merging of earthquake catalogs
Removal of duplicate events
Catalog Processing
Magnitude homogenization
Declustering of the earthquake catalog
Completeness Analysis
Temporal Completeness
Completeness of the earthquake catalog using the Stepp (1972) method
Magnitude Completeness
Estimation of Magnitude of Completeness (M_c)
GMPE Selection and Weighting
Selection of candidate GMPEs
Selection criteria (Bommer et al., 2010; Delavaud et al., 2012)
Weighting of GMPEs (Scherbaum et al., 2009)
Seismicity Analysis for Each Source
Estimation of seismicity parameters
Frequency–magnitude relationship analysis
Seismic activity rate estimation
Delineation of Seismic Sources
Areal source zones
Linear source zones
Point source zones
Logic Tree Framework
Source geometry uncertainty
Seismicity parameter uncertainty
GMPE weighting uncertainty
Probabilistic Seismic Hazard Analysis (PSHA)
PGA and SA hazard maps
Site-specific hazard maps
Uniform Hazard Spectra (UHS)
Result Validation and Applications
Comparison with IS 1893
Comparison with previous PSHA studies
Applications in earthquake engineering

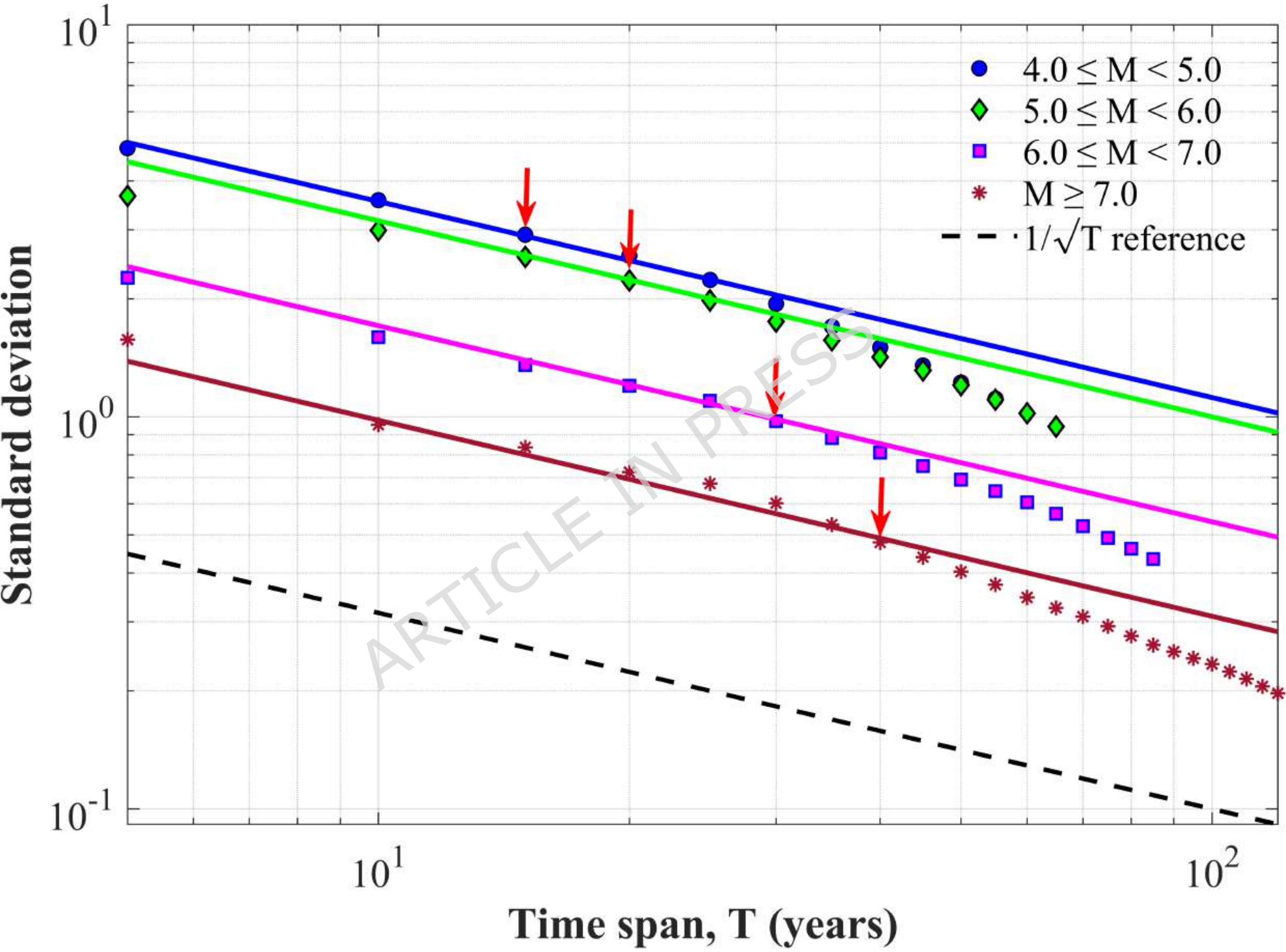

10^{1}
10^{0}
10^{-1}
Standard deviation
$4.0 \leq M < 5.0$
$5.0 \leq M < 6.0$
$6.0 \leq M < 7.0$
$M \geq 7.0$
$1/\sqrt{T}$ reference
10^{1}
10^{2}
Time span, T (years)

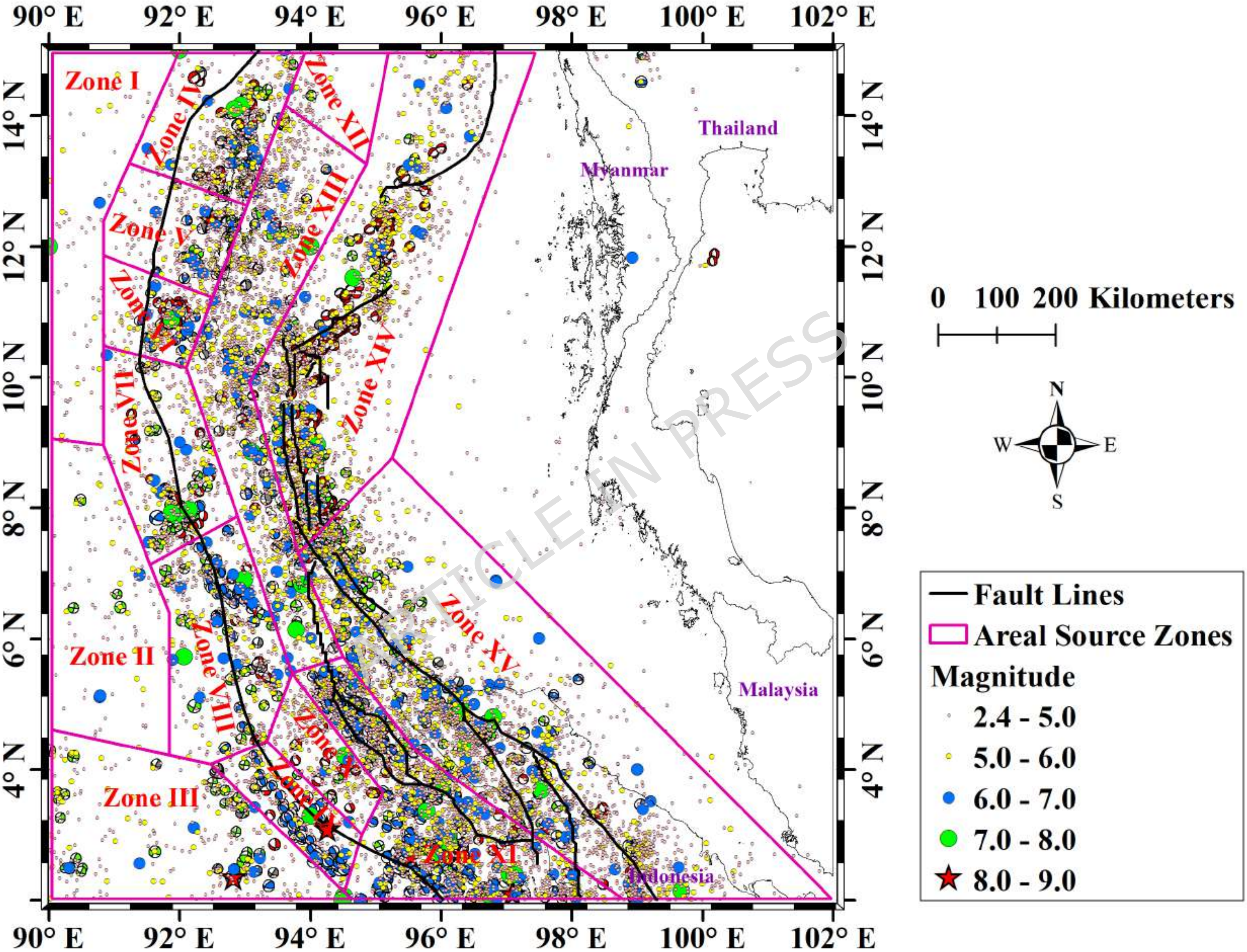

90° E
92° E
94° E
96° E
98° E
100° E
102° E
14° N
12° N
10° N
8° N
6° N
4° N
Zone I
Zone II
Zone III
Zone IV
Zone V
Zone VI
Zone VII
Zone VIII
Zone IX
Zone X
Zone XI
Zone XII
Zone XIII
Zone XIV
Zone XV
Thailand
Myanmar
Malaysia
Indonesia
0 100 200 Kilometers
N
W
E
S
Fault Lines
Areal Source Zones
Magnitude
2.4 - 5.0
5.0 - 6.0
6.0 - 7.0
7.0 - 8.0
8.0 - 9.0

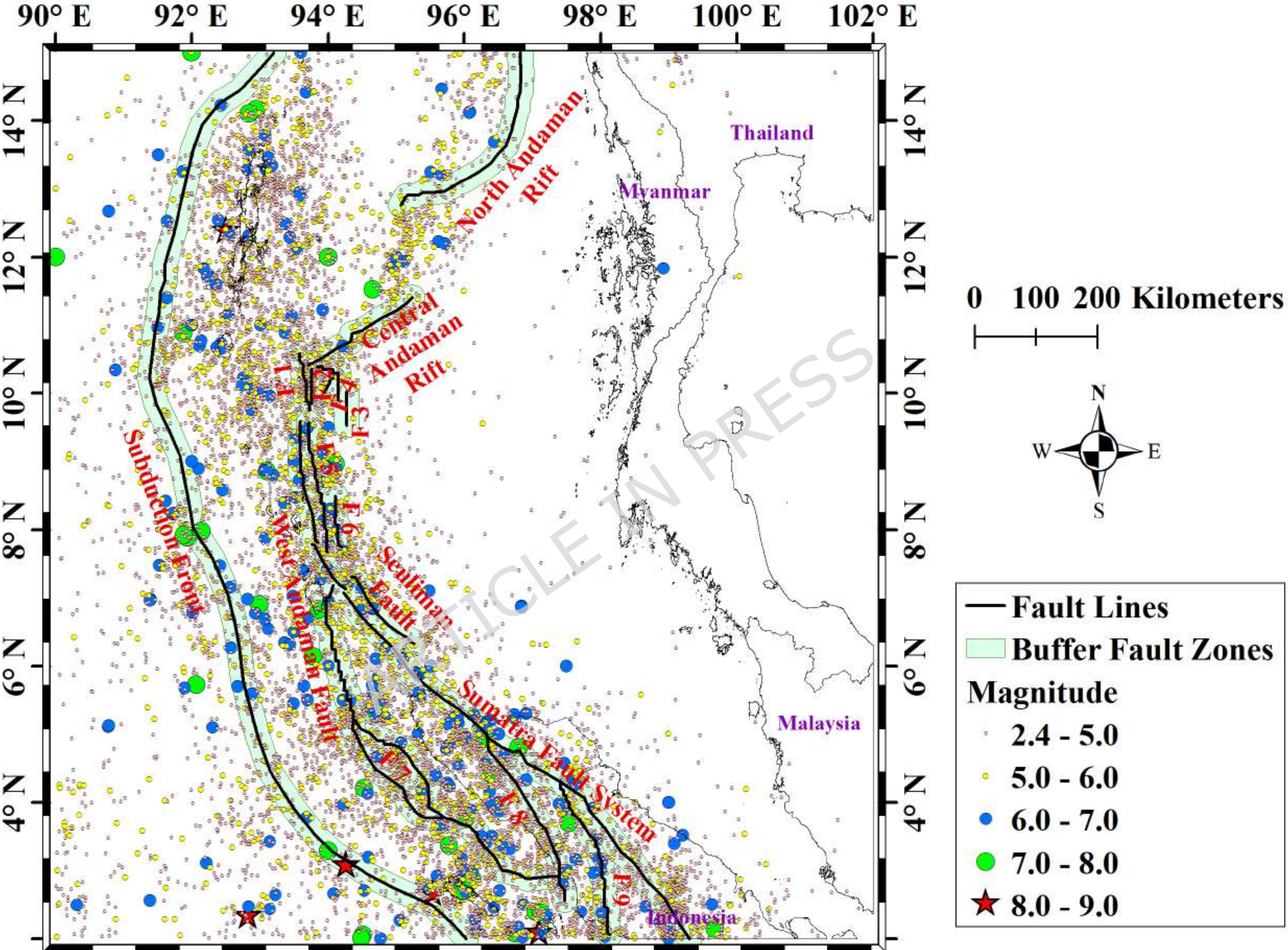

90° E
92° E
94° E
96° E
98° E
100° E
102° E
14° N
12° N
10° N
8° N
6° N
4° N
North Andaman Rift
Central Andaman Rift
Subduction Front
West Andaman Fault
Seulimam Fault
Sumatra Fault System
F1
F3
F5
F6
F7
F8
F9
Thailand
Myanmar
Malaysia
Indonesia
0 100 200 Kilometers
N
S
W
E
Fault Lines
Buffer Fault Zones
Magnitude
2.4 - 5.0
5.0 - 6.0
6.0 - 7.0
7.0 - 8.0
8.0 - 9.0

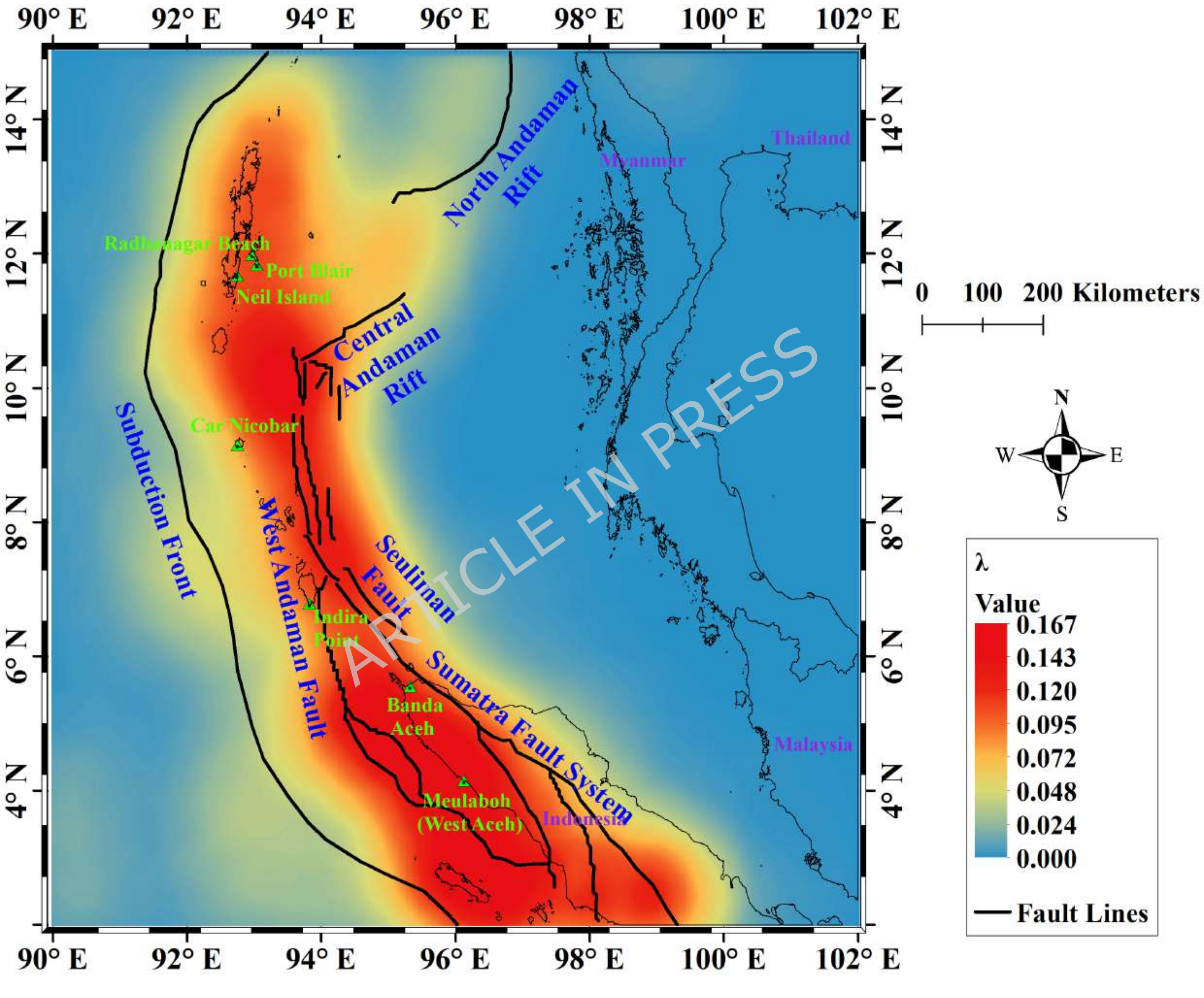
90° E
92° E
94° E
96° E
98° E
100° E
102° E
14° N
12° N
10° N
8° N
6° N
4° N
North Andaman Rift
Central Andaman Rift
Subduction Front
West Andaman Fault
Seulinan Fault
Sumatra Fault System
Radhanagar Beach
Port Blair
Neil Island
Car Nicobar
Indira Point
Banda Aceh
Meulaboh (West Aceh)
Myanmar
Thailand
Malaysia
Indonesia
0 100 200 Kilometers
N
W
E
S
λ
Value
0.167
0.143
0.120
0.095
0.072
0.048
0.024
0.000
Fault Lines

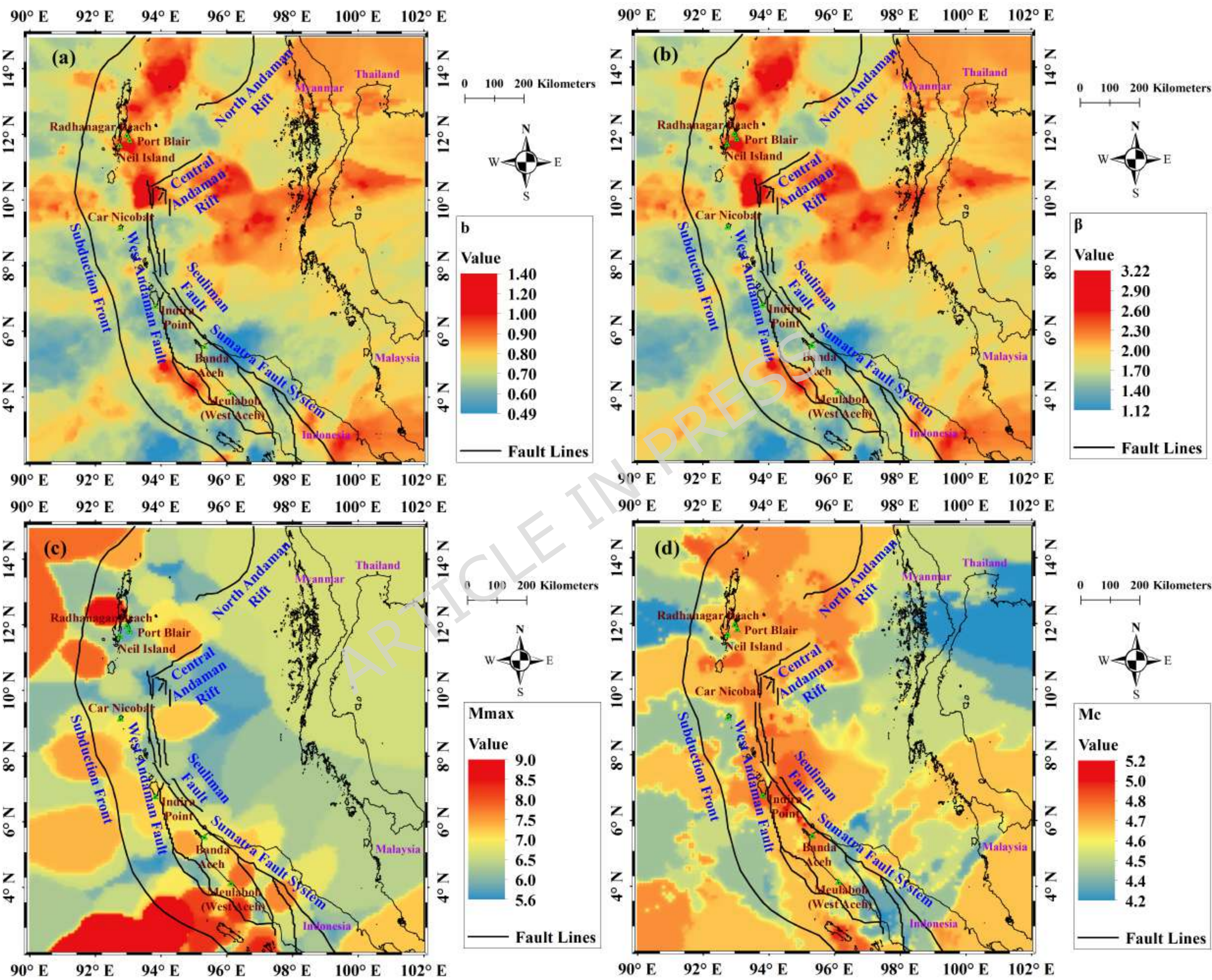

(a)
(b)
(c)
(d)
90° E
92° E
94° E
96° E
98° E
100° E
102° E
4° N
6° N
8° N
10° N
12° N
14° N
Thailand
Myanmar
Malaysia
Indonesia
North Andaman Rift
Central Andaman Rift
Radhanagar Beach
Port Blair
Neil Island
Car Nicobar
Subduction Front
West Andaman Fault
Seuliman Fault
Indira Point
Sumatra Fault System
Banda Aceh
Meulaboh (West Aceh)
0 100 200 Kilometers
N
S
E
W
b
Value
1.40
1.20
1.00
0.90
0.80
0.70
0.60
0.49
Fault Lines
β
Value
3.22
2.90
2.60
2.30
2.00
1.70
1.40
1.12
Fault Lines
Mmax
Value
9.0
8.5
8.0
7.5
7.0
6.5
6.0
5.6
Fault Lines
Mc
Value
5.2
5.0
4.8
4.7
4.6
4.5
4.4
4.2
Fault Lines

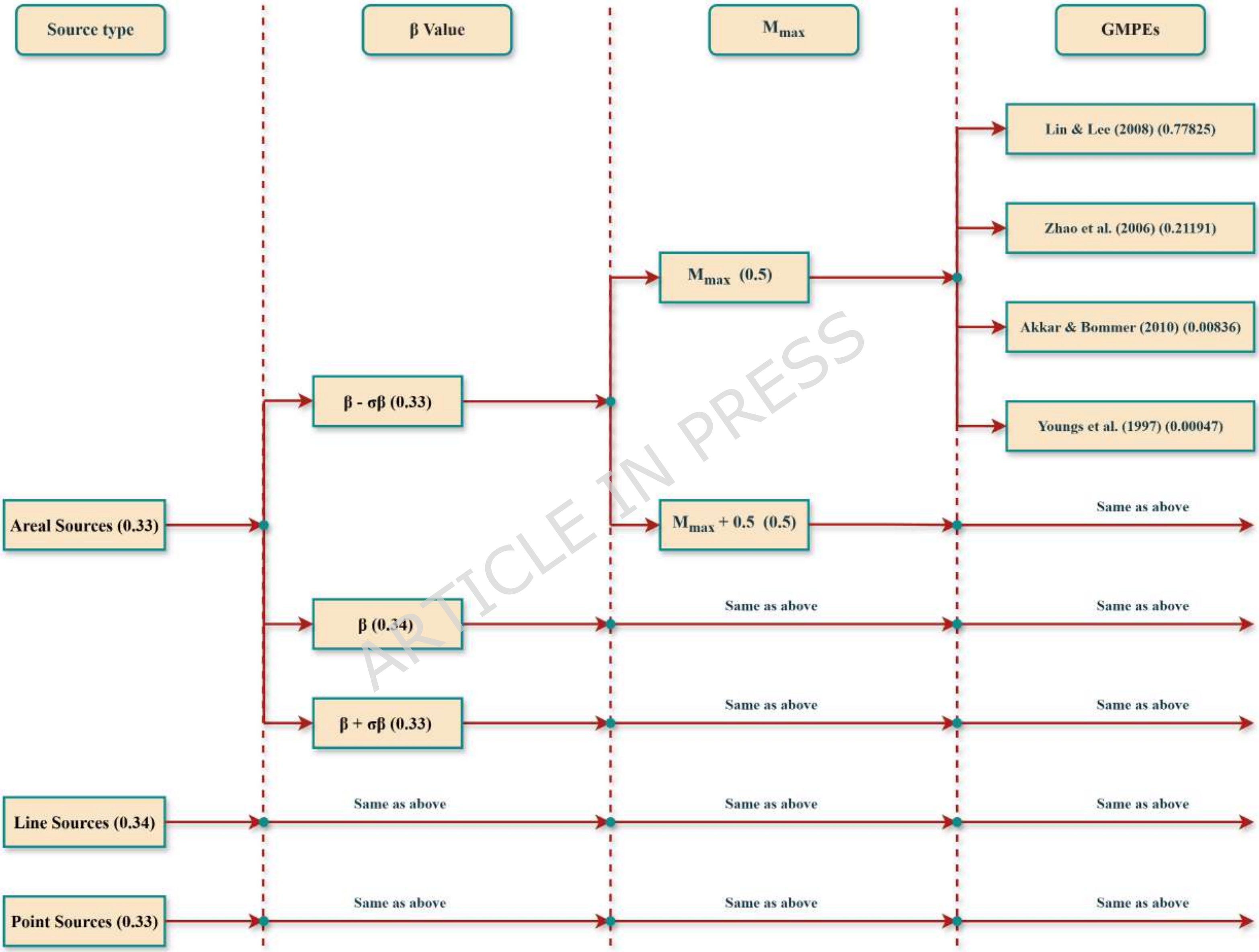

Source type
β Value
M_{max}
GMPEs
Lin & Lee (2008) (0.77825)
Zhao et al. (2006) (0.21191)
M_{max} (0.5)
Akkar & Bommer (2010) (0.00836)
β - σβ (0.33)
Youngs et al. (1997) (0.00047)
Areal Sources (0.33)
M_{max} + 0.5 (0.5)
Same as above
β (0.34)
β + σβ (0.33)
Line Sources (0.34)
Point Sources (0.33)

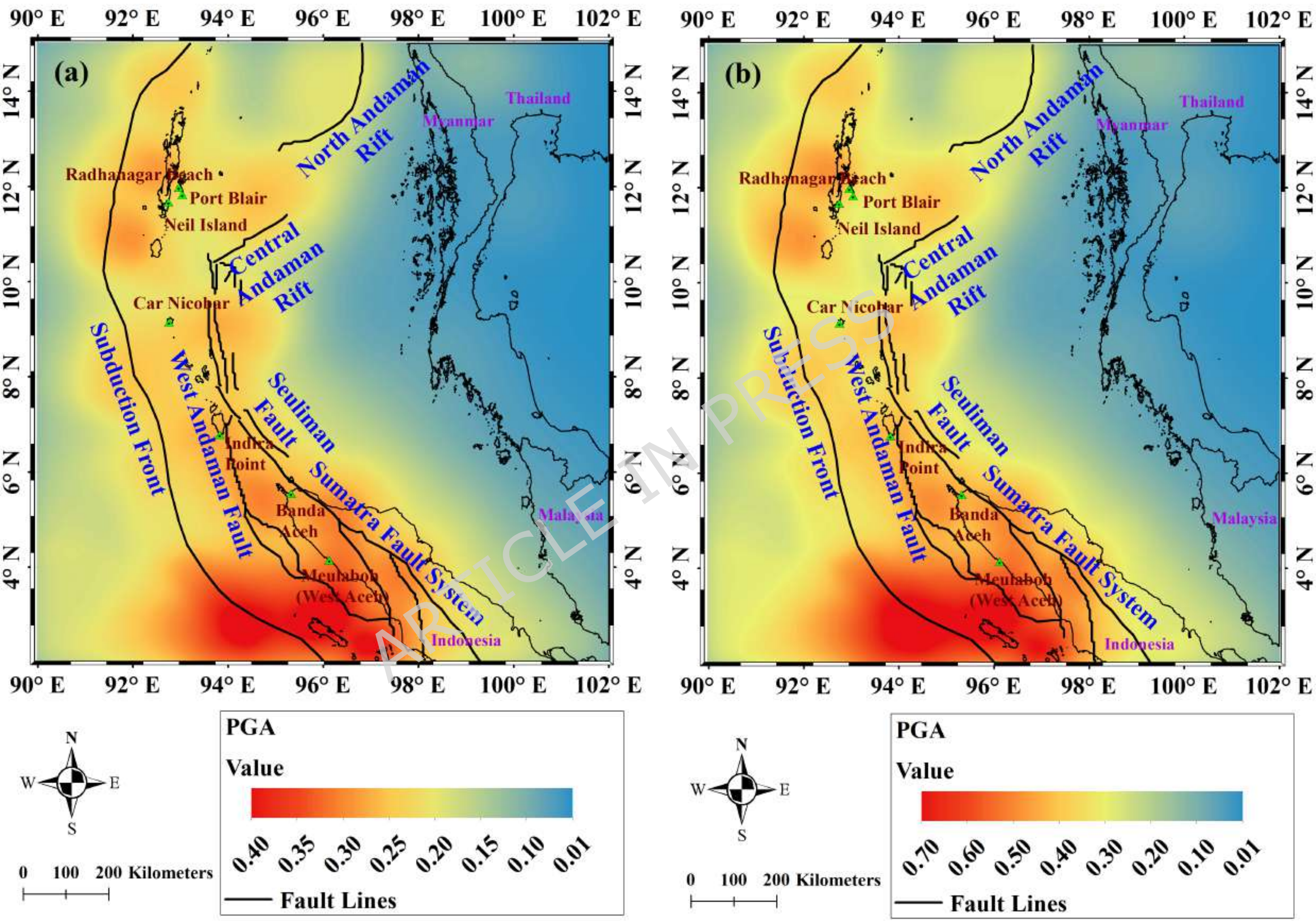

(a)
(b)
Radhanagar Beach
Port Blair
Neil Island
Car Nicobar
Indira Point
Banda Aceh
Meulaboh (West Aceh)
North Andaman Rift
Central Andaman Rift
Subduction Front
West Andaman Fault
Seuliman Fault
Sumatra Fault System
Myanmar
Thailand
Malaysia
Indonesia
PGA
Value
0.40 0.35 0.30 0.25 0.20 0.15 0.10 0.01
0.70 0.60 0.50 0.40 0.30 0.20 0.10 0.01
0 100 200 Kilometers
Fault Lines